The Multi-scale Structure and Development Mechanism of Mesoscale Cyclones over the Sea of Japan in Winter

Kazuhisa TSUBOKI and Tomio ASAI[1]

Ocean Research Institute, University of Tokyo, Tokyo, Japan

(Manuscript received 1 August 2003, in final form 18 November 2003)

Abstract

The western Sea of Japan is a region in which mesoscale cyclones are frequently observed as cold polar air breaks out over the sea. In this region, mesoscale cyclones occasionally develop along a convergence zone that forms on the lee side of the mountains north of the Korean Peninsula. A meso-α-scale cyclone (MαC), in which two meso-β-scale cyclones (MβCs) were embedded, was observed in the western Sea of Japan on 23 January 1990. This structure is referred to as a "multi-scale structure" of a mesoscale cyclone. A simulation experiment and a number of sensitivity experiments with respect to several forcing factors were performed to elucidate the development mechanism of mesoscale cyclones. Stably stratified air flows around the mountains north of the Korean Peninsula and the convergence zone forms on the lee side of the mountains. Large amounts of sensible heat and latent heat are supplied from the sea to the atmosphere. The diabatic heating due to condensation and vertical diffusion of the sensible heat and horizontal advection of the potential temperature θ are almost in balance with the negative vertical advection of θ. This results in an intense upward motion in the convergence zone. Since baroclinicity is intense in this region, an upward transfer of the horizontal momentum around the convergence zone intensifies the upper-level (800~600 hPa) divergence. Consequently, the surface pressure decreases, and the MαC develops. The upward motion and vorticity are concentrated mostly in the MβCs, which are considered to be the cores of the MαC. On the other hand, the MαC provides an environment for the formation and development of the MβCs and affects their movements.

1. Introduction

When continental polar air breaks out over the Sea of Japan in winter, satellite images occasionally show mesoscale cloud vortices in the cold air stream. The vortices with a horizontal scale of several hundred kilometers are referred to as "mesoscale cyclones" or, sometimes, "polar lows." These disturbances yield severe snowstorms and strong gusts of wind along the coastal regions of the Japanese Islands. Their horizontal sizes are smaller than those of synoptic-scale disturbances and larger than a radar processing range. These characteristics make it difficult to reveal the structure and mechanism of the mesoscale cyclones and to predict their formation and development.

Mesoscale cyclones with different horizontal scales are sometimes observed simultaneously. A meso-β-scale cyclone is occasionally embedded in a meso-α-scale cyclone. Ninomiya et al. (1990), and Ninomiya and Hoshino (1990) found this type of structure of a polar low that developed over the Sea of Japan and referred to it as a "multi-scale structure" of the polar low. The development mechanism of this type of polar low and the interaction between meso-

scale cyclones with different scales are still unknown.

Mesoscale cyclones or polar lows are observed in the North Atlantic Ocean, the North Pacific Ocean (Sardie and Warner 1985; Reed 1979; Reed and Blier 1986a, 1986b), the Norwegian Sea, the North Sea, the Barents Sea (Rasmussen and Lystad 1987; Rasmussen 1985; Businger 1985), the Labrador Sea (Moore et al. 1996), the Gulf of Alaska, and the Bering Sea (Businger 1987; Businger and Walter 1988). Ninomiya (1989) called mesoscale cyclones polar lows and showed that they develop frequently over the Sea of Japan and the northwestern Pacific Ocean, where baroclinicity is intense in the low and middle layers of the troposphere.

Asai (1988) showed the frequent appearance of mesoscale cyclones over the Sea of Japan and over the northwestern Pacific Ocean using satellite cloud pictures for the winter period of 1983–1984 (Fig. 1). Most of the mesoscale cyclones were observed in two preferred regions of the Sea of Japan: one is the western Sea of Japan, and the other is off the west coast of Hokkaido Island. These regions correspond to the Japan-Sea Polar-airmass Convergence Zone (JPCZ) (Asai 1988), where broad cloud bands often develop.

The structure and formation process of the cloud band along the JPCZ in the western Sea
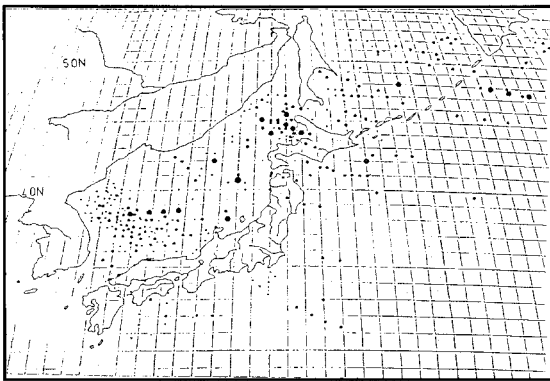

Fig. 1. Geographical distribution of the locations of individual mesoscale cyclones first observed on satellite cloud pictures over the Sea of Japan and its vicinity during the winter of 1983–1984. Larger dots denote larger mesoscale cyclones (adopted from Asai 1988).

of Japan were investigated by Nagata et al. (1986) and Nagata (1987, 1991) using a high resolution numerical model. They showed that the mountains north of the Korean Peninsula (Hamgyong Range and Mt. Changbai), the thermal contrast between the Sea of Japan and the Korean Peninsula, and the characteristic distribution of the sea surface temperature play important roles in producing the cloud band. The mountains are the key topography in the present paper and are referred to hereafter as "Mts.C." These numerical experiments showed the structure and characteristics of the JPCZ though no mesoscale cyclone was investigated. The most distinct characteristic of the mesoscale cyclones over the Sea of Japan in winter is that most of them develop along the JPCZ.

Many studies have been conducted to explain the mechanisms of the cyclogenesis and development of polar lows and mesoscale cyclones. Powerful approaches to explain the scale selection of a cyclone are linear instability theories. Two types of hydrodynamic instability of atmospheric flows are considered to be important for the mechanisms of a polar low genesis: one is baroclinic instability (Harrold and Browning 1969; Mansfield 1974; Duncan 1977; Reed and Duncan 1987), and the other is conditional instability of the second kind (CISK) (Rasmussen 1979; Bratseth 1985; Økland 1987; Craig and Cho 1988). Tsuboki and Wakahama (1992) found two unstable baroclinic modes with reduced static stability of the lower atmosphere around the JPCZ off the west coast of Hokkaido that corresponded to two types of observed mesoscale cyclones. Iga (1997) applied the linear instability theory of frontal waves (Orlanski 1968; Iga 1993) to the convergence zone and discussed the characteristics of the unstable mode with a layer of uniform potential vorticity. The linear instability theories, however, seem to be difficult to explain the development mechanism of the mesoscale cyclones in the western Sea of Japan, because the mesoscale cyclones in the present paper develop along the JPCZ with preexisting finite amplitude vorticity and convergence. Emanuel and Rotunno (1989) applied a theory of finite-amplitude air-sea interaction instability (Emanuel 1986) to explain the minimum sustainable central pressure of polar lows in a steady state. On the

other hand, the development process of meso-scale cyclones will be studied in the present study.

The mesoscale cyclones in the western Sea of Japan seem to be influenced by many forcing factors, such as the topography, the intense heat flux from the sea, and the convergence zone. In this study, we examine the development mechanism from the viewpoint of the surface pressure tendency equation in the pressure coordinate

$$\frac{\partial p_s}{\partial t} = -\mathbf{V_s} \cdot \nabla p_s - \int_0^{p_s} \nabla_p \cdot \mathbf{V_h}\, dp, \qquad (1)$$

where p_s is the surface pressure, $\mathbf{V_s}$ is the surface velocity, and $\mathbf{V_h}$ is the horizontal velocity. According to (1), the development of a surface low is related to the upper-air divergence.

A meso-α-scale cyclone (MαC) and two meso-β-scale cyclones (MβCs) were observed simultaneously over the western Sea of Japan on 23 January 1990. The objectives of the present paper are to reveal the multi-scale structure of mesoscale cyclones and clarify their development mechanism. A simulation experiment of mesoscale cyclones and a number of sensitivity experiments with respect to several forcing factors were performed with the use of a limited-area spectral model. According to the results of these experiments, the development mechanism of the MαC, the interaction between the MαC and the MβCs, and the role of the MβCs in the development process of the MαC will be discussed.

2. Data and model

2.1 Data

The following data for the period from 21 to 24 of January 1990, which were provided by the Japan Meteorological Agency (JMA), were used for data analyses and numerical experiments:

1. Objective analysis data of the area of Japan and its surroundings (JANAL) with a resolution of 80 km (at 60°N) at the surface, and at 850, 700, 500, 400, 300, 250, 200, 150, 100, 70, 50, 30, 20, and 10 hPa every 12 hours,
2. Daily analysis of the sea surface temperature (SST) with a resolution of 1.0 degree in both latitude and longitude,
3. Geostationary Meteorological Satellite (GMS) infra-red (IR) images,

4. Radar images at Fukui and Niigata observatories of JMA, and
5. Daily weather charts.

The JANAL data were interpolated into model grids and used for initial and boundary conditions of the numerical simulation and sensitivity experiments. The SST data were used for a lower boundary condition in sea areas.

2.2 Model

The Japan Spectral Model (JSM) of the 1988 version is used for the present numerical study of mesoscale cyclones. JSM is a spectral limited-area model developed by JMA for operational forecasts (Segami et al. 1989). The model is formulated in terms of the primitive equations in sigma coordinates. The spectral method with a time-dependent lateral boundary condition (Tatsumi 1986) is used in the model. The vertical levels are 23 sigma levels in this study. The transform grids are 129 points each in the x and y directions. The horizontal spacing of model grids is chosen to be 30 km for the present study. The domain of the numerical simulation and sensitivity experiments is shown in Fig. 2. The rectangle to the north of the Korean Peninsula indicates Mts.C. The map projection is the north polar stereo-graphic projection. The distribution of the sea surface temperature is fixed throughout the time-integration period.

Moist processes in the model indicate the moist convective adjustment for subgrid-scale convection, grid-scale condensation, and evaporation of raindrops. Surface fluxes are calculated by a bulk method. The level-2 version of the turbulent closure model (Mellor and Yamada 1974) is used for vertical diffusion. Ground temperature is calculated by a four-layer model. Radiation is taken into account only for the calculation of the ground temperature.

3. Mesoscale cyclones on 23 January 1990

A developing extratropical cyclone passed over the Sea of Japan NE-ward on 22 January 1990 and then there was an outburst of cold air over the Sea of Japan. The weather chart at 1200 UTC, 23 January 1990 (Fig. 3a) shows that a cold northerly spread over the Sea of
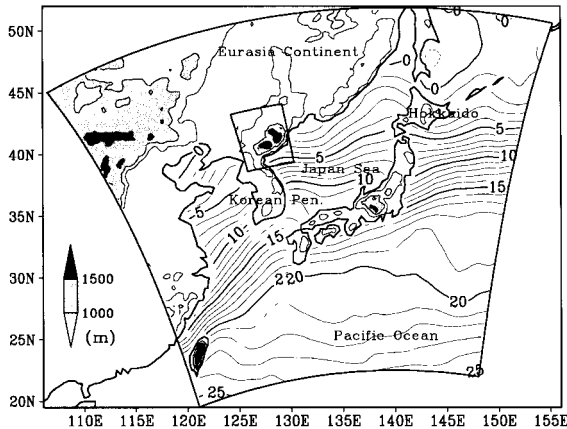
Fig. 2. Domain of numerical simulation and sensitivity experiments, topography, and the sea surface temperature on 21 January 1990. The rectangle to the north of the Korean Peninsula in the figure indicates the region of topography modification in a sensitivity experiment. The lowest contour lines of the topography indicate 500 m in altitude. The lightly shaded regions are areas higher than 1000 m, and the darkly shaded regions are higher than 1500 m in altitude.

Japan at the surface. A convergence zone formed in the western Sea of Japan between the northerly and the northwesterly from the Korean Peninsula. A mesoscale low is found around 136°E and 37°N. This is the MαC referred to in this paper.

The temperature and height fields at 500 hPa (Fig. 3b) show the typical patterns observed when there is an outburst of cold air over the Sea of Japan. An intense cold low is located to the NW of Japan and the westerly prevails over the Sea of Japan. The significant rotation of wind direction with height indicates intense baroclinicity over the Sea of Japan. This is a characteristic of the environment for the development of the MαC.

A time series of satellite images of GMS is shown in Fig. 4 for the period from 1000 to 2000 UTC, 23 January 1990. A broad cloud band with a width of 200~300 km extends from the NW to the SE along the convergence zone over the Sea of Japan on the lee side of Mts.C (Fig. 4a). A narrow convective cloud band is
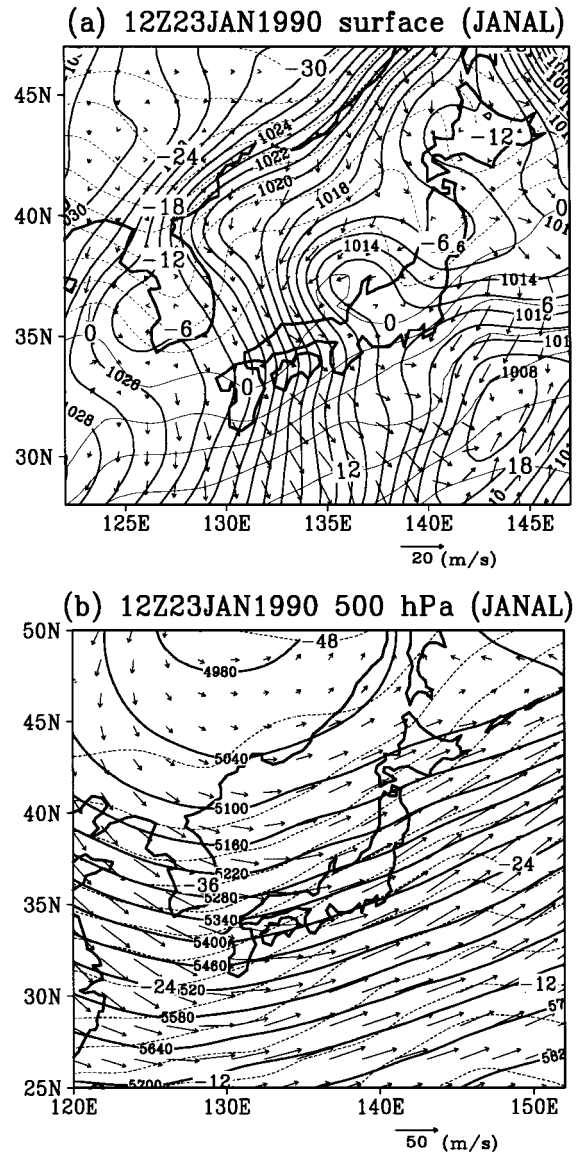

Fig. 3. Synoptic maps at 1200 UTC, 23 January 1990 of (a) pressure (thick lines; unit is hPa), temperature (thin lines; °C), and wind (arrows) at the surface, and (b) height (thick lines; meter), temperature (thin lines; °C), and wind (arrows) at 500 hPa obtained from the JMA objective analysis. Solid lines indicate positive values, and dashed lines, negative values. The arrow scales (m s⁻¹) of wind are shown at the bottom of each figure.
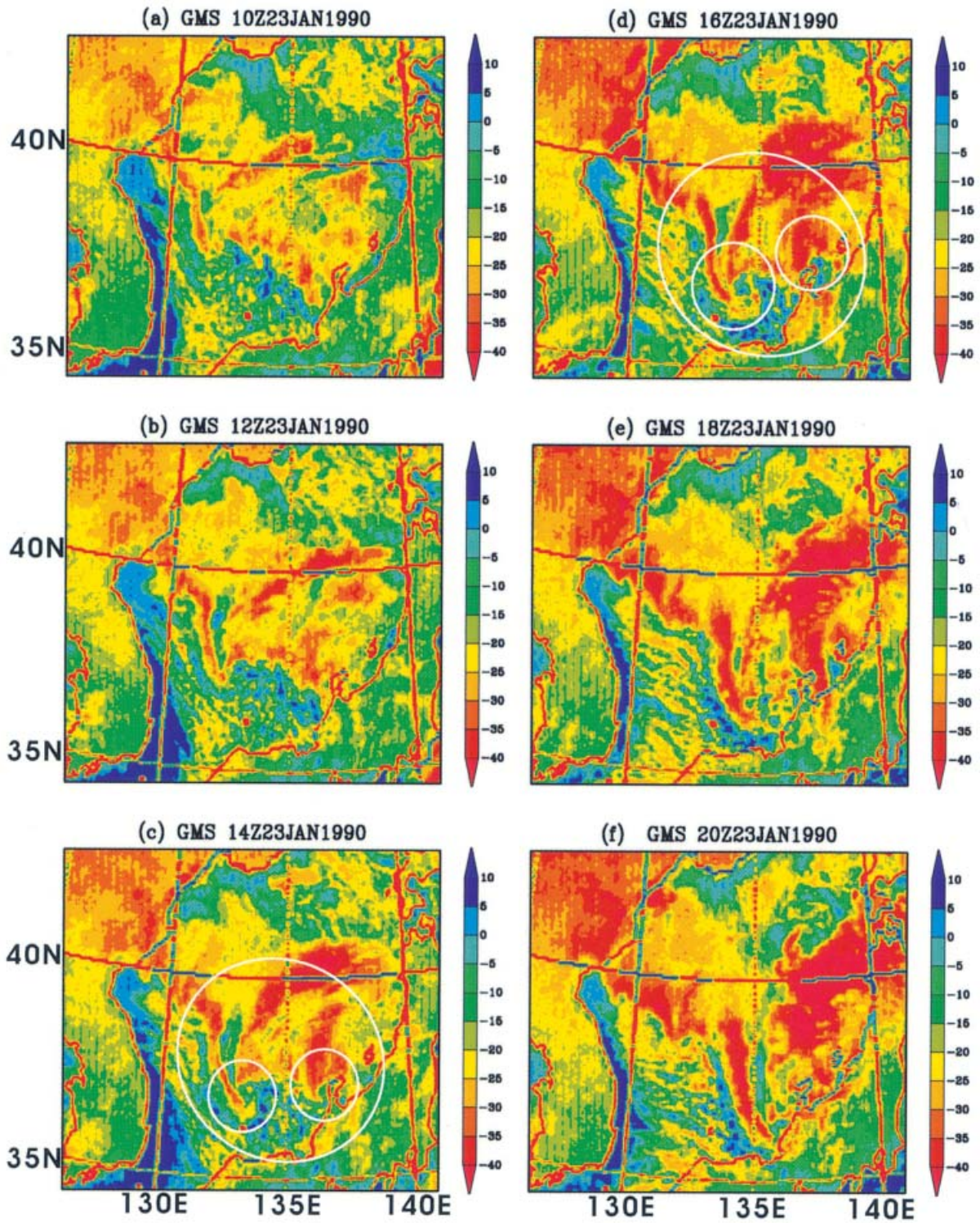
Fig. 4. Time series of the GMS infrared images every two hours for the period from 1000 to 2000 UTC, 23 January 1990. The color levels of TBB (°C) are shown on the right-hand side of each figure. The large oval indicates the meso-α-scale cyclone (MαC), and the two small ovals, the meso-β-scale cyclones (MβCs) in (c) and (d).

found along the west edge of the broad cloud band. Transversal cloud bands extending to the NE from the narrow convective cloud band are embedded in the broad cloud band. A meso-α-scale vortical cloud with a horizontal scale of several hundred kilometers began to develop in the broad cloud band at 1200 UTC, 23 January (Fig. 4b). This corresponds to the MαC shown in the surface weather chart (Fig. 3a). An intense arc-shaped cloud extended from the west side of the broad cloud band to the NE.

At 1400 UTC, 23 January (Fig. 4c), two meso-β-scale vortical clouds aligned in the west-east direction and became distinct within the MαC. These correspond to the MβCs. One of them located at 136.5°E and 37°N will be hereafter referred to as the "MβC-A" and the other, located at 133°E and 37°N, as the "MβC-B." The MβC-A moved to the ENE, while the MβC-B moved to the SE (Figs. 4d and 4e). The center of the MαC is obscure in comparison with the vortex patterns of the MβCs. It is the most important point in this study that the two MβCs are embedded in the MαC. The MβCs landed over the Japanese Islands around 2000 UTC, 23 January 1990, and these vortex cloud patterns disappeared (Fig. 4f). The broad cloud band remained over the Sea of Japan after the vortices of cloud disappeared.

Precipitation patterns associated with the MβCs and their movements are observed by the JMA meteorological radars when they come close to the Japanese Islands. The precipitation echo of the broad cloud band was observed off the coast at 1000 UTC, 23 January 1990 (Fig. 5a). A spiral echo of the MβC-A began to develop with a center at 136°E and 37°E at 1200 UTC, 23 January (Fig. 5b). The spiral echo pattern of the MβC-A became clear and moved to the ENE along the coast (Figs. 5c and 5d). The other spiral echo of the MβC-B came into the radar range at 1600 UTC, 23 January (Fig. 5d). The MβC-B moved SE-ward (Figs. 5d, 5e, and 5f). Both the MβCs-A and -B landed over the Japanese Islands at 2000 UTC, 23 January (Fig. 5f) and then disappeared. These vortices had a horizontal scale of about 200∼300 km and were accompanied by intense precipitation. Ookubo (1995) also studied these meso-β-scale vortices and revealed their detailed structure and different movements of the two vortices; one moved ENE-ward, and the other, SE-ward.

4. Simulation experiment

4.1 Time variation of disturbances

The simulation was started at 0000 UTC, 22 January 1990, which is 36 hours before the MαC fully develops, and was terminated at 0000 UTC, 24 January 1990. In the initial field (not shown), the synoptic-scale low was present over the Sea of Japan and moved NE-ward. The convergence zone and the mesoscale cyclones were not observed in the initial field.

The simulation experiment showed an outburst of cold air over the sea after the synoptic-scale low moved NE-ward over the Sea of Japan. The convergence zone in the cold air stream formed on the lee side of Mts.C and extended to the Japanese Islands over the Sea of Japan. The mesoscale cyclones then developed along the convergence zone.

Figure 6 shows time-height cross-sections of horizontal divergence and vorticity averaged in 132–137°E, 35.5–38.5°N, where the MαC develops. Figure 6a shows that the lower-level convergence below 850 hPa and upper-level divergence between 850 hPa and 500 hPa are significantly intense after 08 UTC, 23 January. The averaged vorticity (Fig. 6b) increases with time below 600 hPa. Corresponding to the intense divergence, the vorticity is intense during the period from 08 to 19 UTC, 23 January. This indicates that the mesoscale cyclones develop and are the most intense during this period. The vorticity is almost constant with time in the layer from 600 to 450 hPa. This indicates that the mesoscale cyclones are confined to below the 600 hPa level.

4.2 The convergence zone in the western Sea of Japan

When the synoptic-scale low is located to the NE of the Sea of Japan, the cold northerly from the Eurasia Continent and the northwesterly from the Korean Peninsula prevail over the Sea of Japan (Fig. 7). The convergence zone forms between these two flows around 00 UTC, 23 January 1990, and a precipitation band develops along the convergence zone. A mesoscale ridge forms to the NE of the convergence zone (Fig. 7a). The northwesterly from the continent rotates clockwise toward the convergence zone over the mesoscale ridge.

At 860 hPa (Fig. 7b), a NE-ward flow is present on the NE side of the precipitation band

(a)   10Z23JAN1990

(d)   16Z23JAN1990

(b)   12Z23JAN1990

(e)   18Z23JAN1990
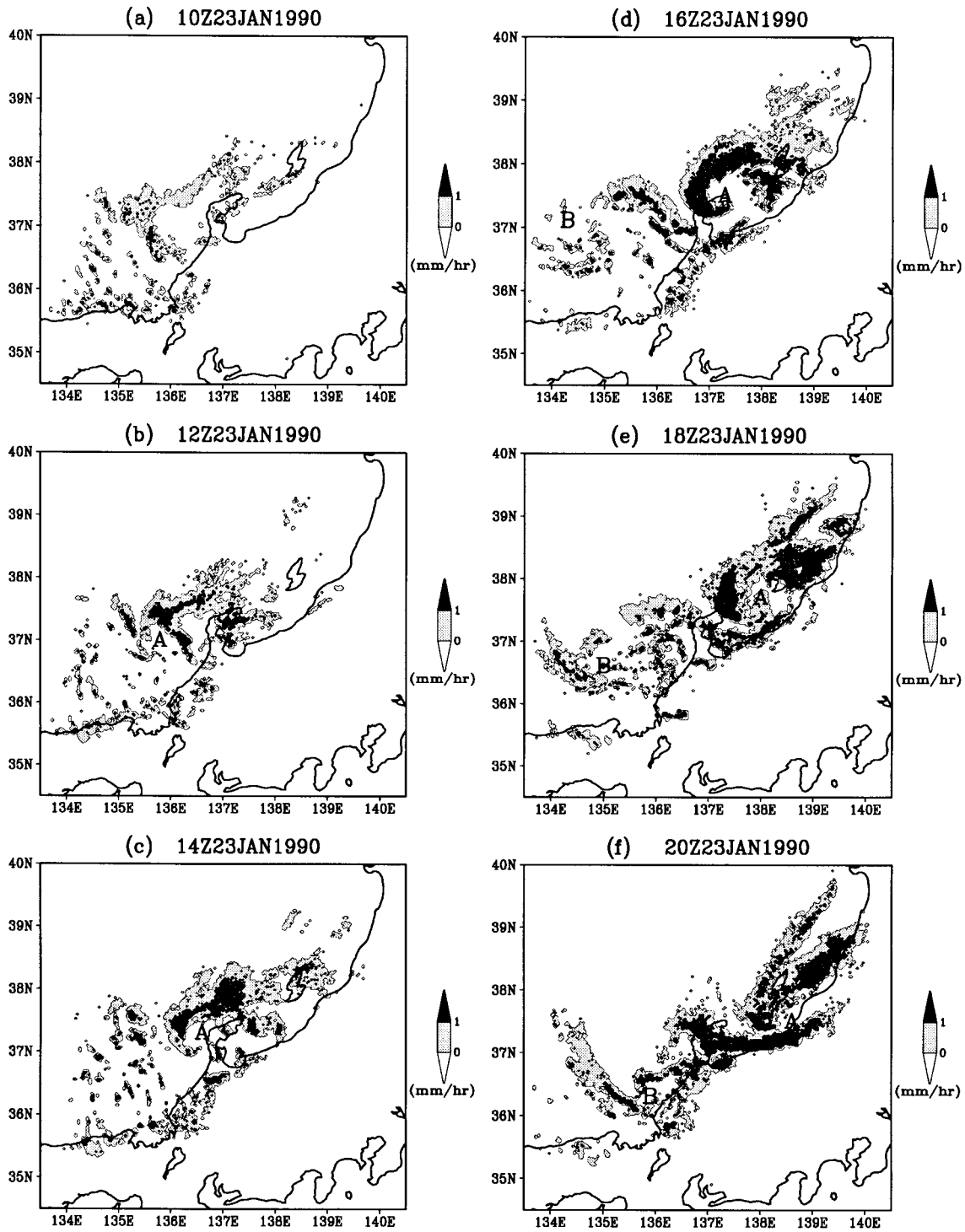
(c)   14Z23JAN1990

(f)   20Z23JAN1990

Fig. 5.   Time series of a composite echo map of the Fukui and Niigata meteorological radars every two hours for the period from 1000 to 2000 UTC, 23 January 1990. Echo levels (mm hr^{-1}) are shown on the right-hand side of each figure. The centers of MβCs-A and -B are indicated by "A" and "B" in the figures, respectively.
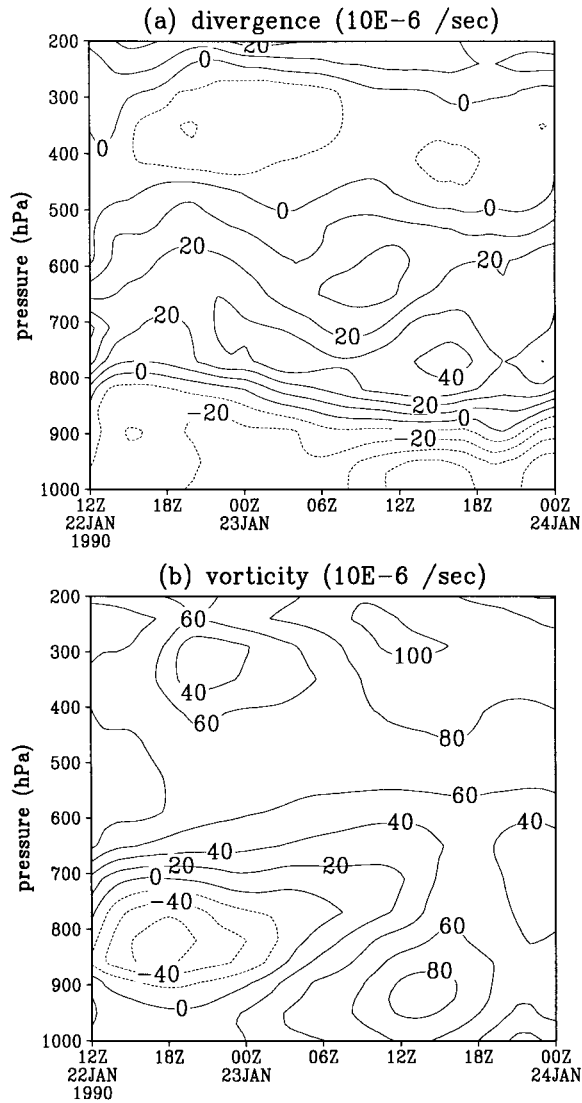
Fig. 6. Time-height cross-sections of (a) averaged divergence (unit is 10^{-6} s^{-1}) and (b) averaged vorticity (unit is 10^{-6} s^{-1}) in the area of 132–137°E, 35.5–38.5°N obtained from the simulation experiment.
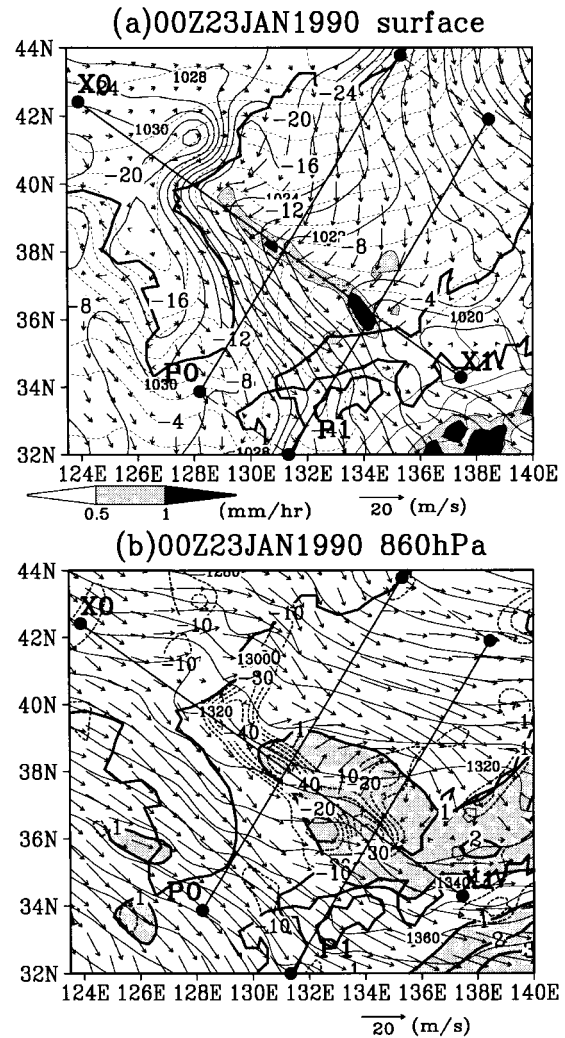

Fig. 7. Horizontal displays of the simulated fields at 0000 UTC, 23 January 1990. (a) Surface pressure (thick lines; unit is hPa), surface wind (arrows; m s^{-1}), temperature of 1000 hPa (thin lines; °C), and precipitation intensity (shading; mm hr^{-1}), and (b) height (thin solid lines; meter), specific humidity (thick solid lines; g kg^{-1}), upward motion (dashed lines; hPa hr^{-1}), and wind (arrows; m s^{-1}) at a level of 860 hPa. Specific humidity larger than 1 g kg^{-1} is shaded.

within the synoptic-scale northwesterly. This flow is significantly ageostrophic and relatively moist. The ageostrophic flow arises from the upward motion along the precipitation band and extends NE-ward about 200 km horizontally. This indicates that the lower-level moist air is lifted up by the upward motion. The pressure gradient force accelerates the lifted air-parcels NE-ward, and the ageostrophic flow develops.

In order to examine and display the vertical structure of the convergence zone, we define the x and y coordinates as the directions parallel and normal to the convergence zone, respectively (see Fig. 7). The vertical cross-sections

along the x-direction ($X0 - X1$ in Fig. 7) are shown in Fig. 8. The potential temperature and specific humidity (Fig. 8a) show a rapid modification of the continental airmass over the Sea of Japan due to large amounts of sensible heat and latent heat supplied from the sea. The mixing layer of nearly neutral static stability develops immediately when the cold airmass arrives over the sea and the top of the layer reaches the level of 800~700 hPa around Japan. Since the atmosphere over the continent is very stable, Mts.C effectively deflect the lower-level flow, which results in lower-level convergence on the lee side of Mts.C (Fig. 8b). Upper-level divergence occurs in the layer from 900 to 650 hPa above the convergence. Upward motion is associated with the lower-level convergence and upper-level divergence along the convergence zone (Fig. 8c). The condensation in the upward motion and vertical diffusion of sensible heat occur below the level of 700 hPa (Fig. 8d). The convergence zone coincides with a belt of positive vorticity (Fig. 8e). The layer of the positive vorticity is shallow before the mesoscale cyclones develop. The negative x-component of velocity was caused by the clockwise rotation of the lower-level wind over the mesoscale ridge (Fig. 8f).

The vertical structure of the convergence zone normal to the precipitation band is shown in Fig. 9. The convergence zone is centered around 500 km of the abscissa. As shown in Fig. 9a, the convergence zone forms between two airmasses below 850 hPa. The lower-level convergence and upper-level divergence are intense in the convergence zone, accompanying the intense upward motion (Figs. 9b and 9c). Secondary weak upward motion is present on the right-hand side (NE side) of the main upward motion. Since the upward motions lift up the lower-level moisture, the height of the moist layer significantly increases around the convergence zone (Fig. 9a). Diabatic heating is intense around the convergence zone, which extends to 700 hPa (Fig. 9d). Large values of positive vorticity are confined in the convergence zone below 800 hPa, with a width of about 100 km (Fig. 9e). Large values of negative vorticity are found in the layer from the surface to 700 hPa, with a maximum at 850 hPa on the NE side (the right-hand side) of the convergence zone. This is a characteristic fea-

ture of flow when the convergence zone forms. This negative vorticity existed until the MαC generated. The negative component of ageostrophic velocity is significant below 900 hPa on the NE side of the convergence zone, which causes the intense lower-level convergence (Fig. 9f). Above this flow, a positive component of ageostrophic velocity is present between 700 and 900 hPa, which made the upper-level divergence. A weakly stable and moist layer is present above the airmass on the NE side of the convergence zone. This moist layer is considered to correspond to the transversal cloud lines in the broad cloud band observed in the GMS image (Fig. 4a).

Aerological observations of the convergence zone were made by Arakawa et al. (1988) using a research vessel in the western Sea of Japan. They showed a vertical structure of the convergence zone that formed on the lee side of Mts.C (Fig. 10). The convergence zone was observed around from 03 to 09 JST, 5 February 1986. Assuming a steady state of the convergence zone, the time axis can be converted to the horizontal distance. The wind shift below 900 hPa and the vertical motion were significant during this period (Fig. 10a). Another upward motion above 850 hPa was observed after 09 JST. High θ_e (equivalent potential temperature) region was observed between the upper and lower discontinuity lines (Fig. 10b). The structure of the convergence zone in the simulation experiment is similar to that observed by Arakawa et al. (1988) over the Sea of Japan on 4–5 February 1986.

4.3 The mesoscale cyclones

The surface pressure field at 1200 UTC, 23 January 1990 (Fig. 11a) shows the MαC with a horizontal scale of 500~700 km around 135°E and 37°N. Its central pressure is 1016 hPa, and the cyclone is slightly elongated along the convergence zone. The wind on the SW side of the cyclone is northwesterly. On the other hand, the northwesterly to the NE of the convergence zone turns to northeasterly or easterly over the mesoscale ridge on the NE side of the MαC. The precipitation is intense at the central part of the MαC and along the convergence zone.

At 820 hPa (Fig. 11b), an anticyclonic circulation is present to the north of the center of the MαC. The wind direction is almost oppo-
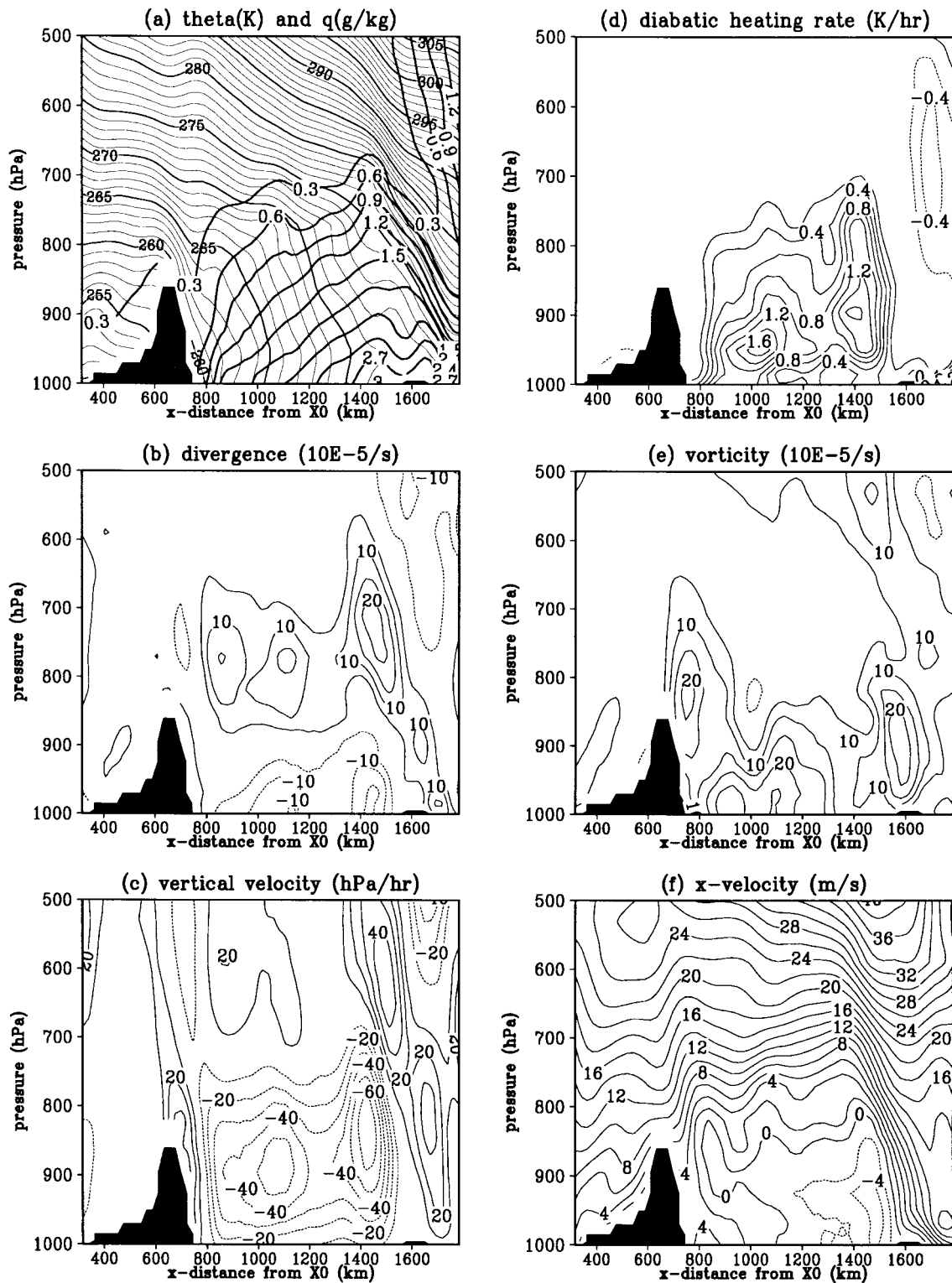
Fig. 8. Vertical cross-sections along the line $X0 - X1$ in Fig. 7 at 0000 UTC, 23 January 1990. (a) Potential temperature (thin lines; K) and specific humidity (thick lines; g kg^{-1}), (b) horizontal divergence (10^{-5} s^{-1}), (c) vertical velocity (hPa hr^{-1}), (d) diabatic heating rate due to the moist processes and vertical diffusion (K hr^{-1}), (e) vorticity (10^{-5} s^{-1}), and (f) x-component of velocity (m s^{-1}). Shading in the figures indicates mountains.
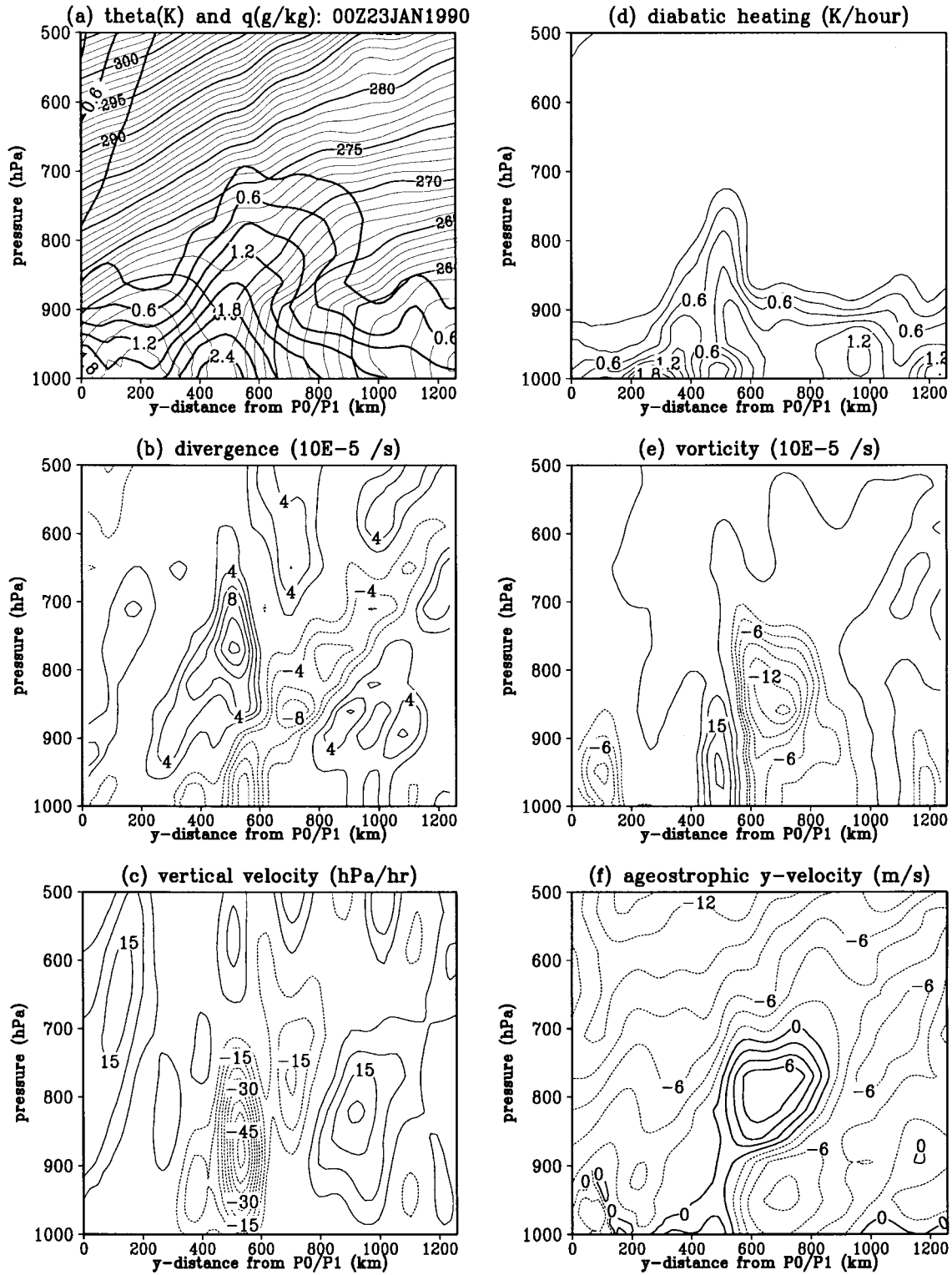
Fig. 9. Vertical cross-sections normal to the precipitation band at 0000 UTC, 23 January 1990. Values are averaged in the x-direction from $P0$ to $P1$ in Fig. 7. (a) Potential temperature (thin lines; K) and specific humidity (thick lines; g kg^{-1}), (b) horizontal divergence (10^{-5} s^{-1}), (c) vertical velocity (hPa hr^{-1}), (d) diabatic heating rate due to the moist processes and vertical diffusion (K hr^{-1}), (e) vorticity (10^{-5} s^{-1}), and (f) y-component of ageostrophic velocity (m s^{-1}).
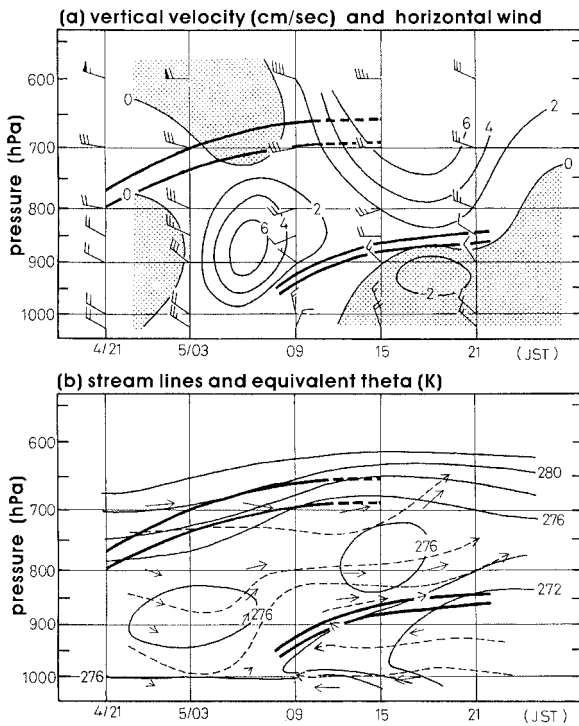
Fig. 10. Time-height cross-sections of (a) horizontal velocity (half barb indicates 5 knots; full barb, 10 knots; and flag, 50 knots) and vertical velocity (cm s^{-1}) and (b) equivalent potential temperature θ_e (solid lines; K) and stream lines (dashed lines) in the vertical cross-section. The shaded areas in (a) indicate downward motion. The thick double lines show discontinuity of temperature. The abscissa is the time according to the Japan Standard Time (JST = UTC + 9) (adopted from Arakawa et al. 1988).

Fig. 11. Horizontal displays of simulated fields at 1200 UTC, 23 January 1990. (a) Surface pressure (solid lines; hPa), surface wind (arrows; m s^{-1}), temperature of 1000 hPa (dashed lines; °C), and precipitation intensity (shadings; mm hr^{-1}). The gray scale is shown at the bottom of the figure. (b) Height (solid lines; meter), temperature (dashed lines; °C), and wind (arrows; m s^{-1}) at a level of 820 hPa.

site to the direction of the geostrophic flow above the MαC. Since the synoptic-scale temperature increases toward the downstream direction of the geostrophic flow, the ageostrophic flow causes warm air advection over the MαC.

Vertical cross-sections in the x-direction ($X0 - X1$ in Fig. 11) show the vertical structure of the MαC (Fig. 12). The mixing layer develops up to ~700 hPa over the Sea of Japan (Fig. 12a) by vertical diffusion of sensible heat and condensation heating (Fig. 12d). The significant upper-level divergence (900~600 hPa) is found in the area where the MαC develops (Fig. 12b), and the upward motion is also intense (Fig. 12c). A maximum of the upward motion at 1400
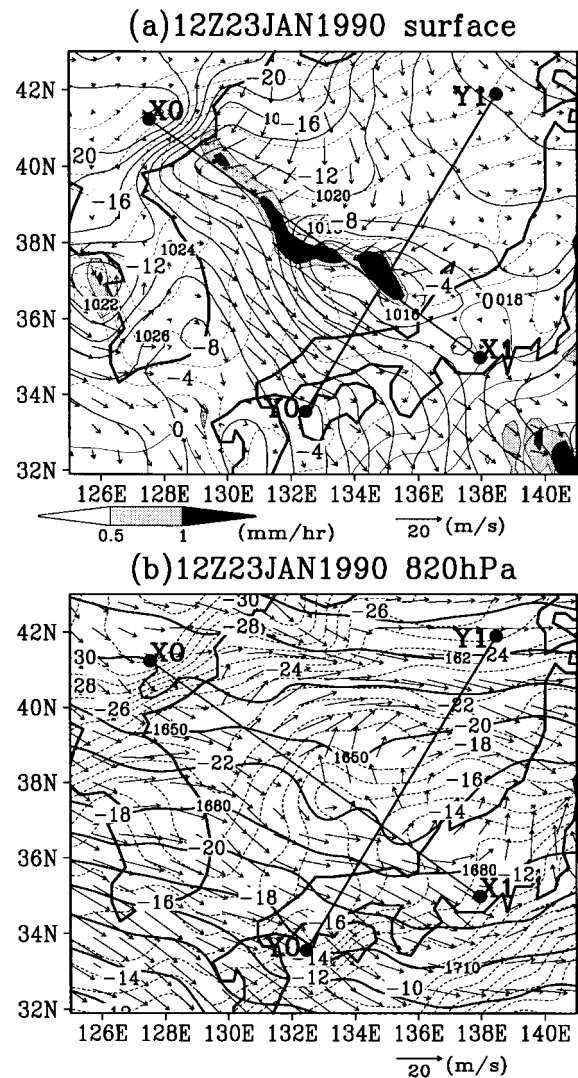
km of the abscissa and another maximum of upward motion at 1250 km have a horizontal scale of about 200 km. These upward motions are considered as cores of the MαC disturbance and have a horizontal scale of MβCs. Corresponding to the upward motion, the diabatic
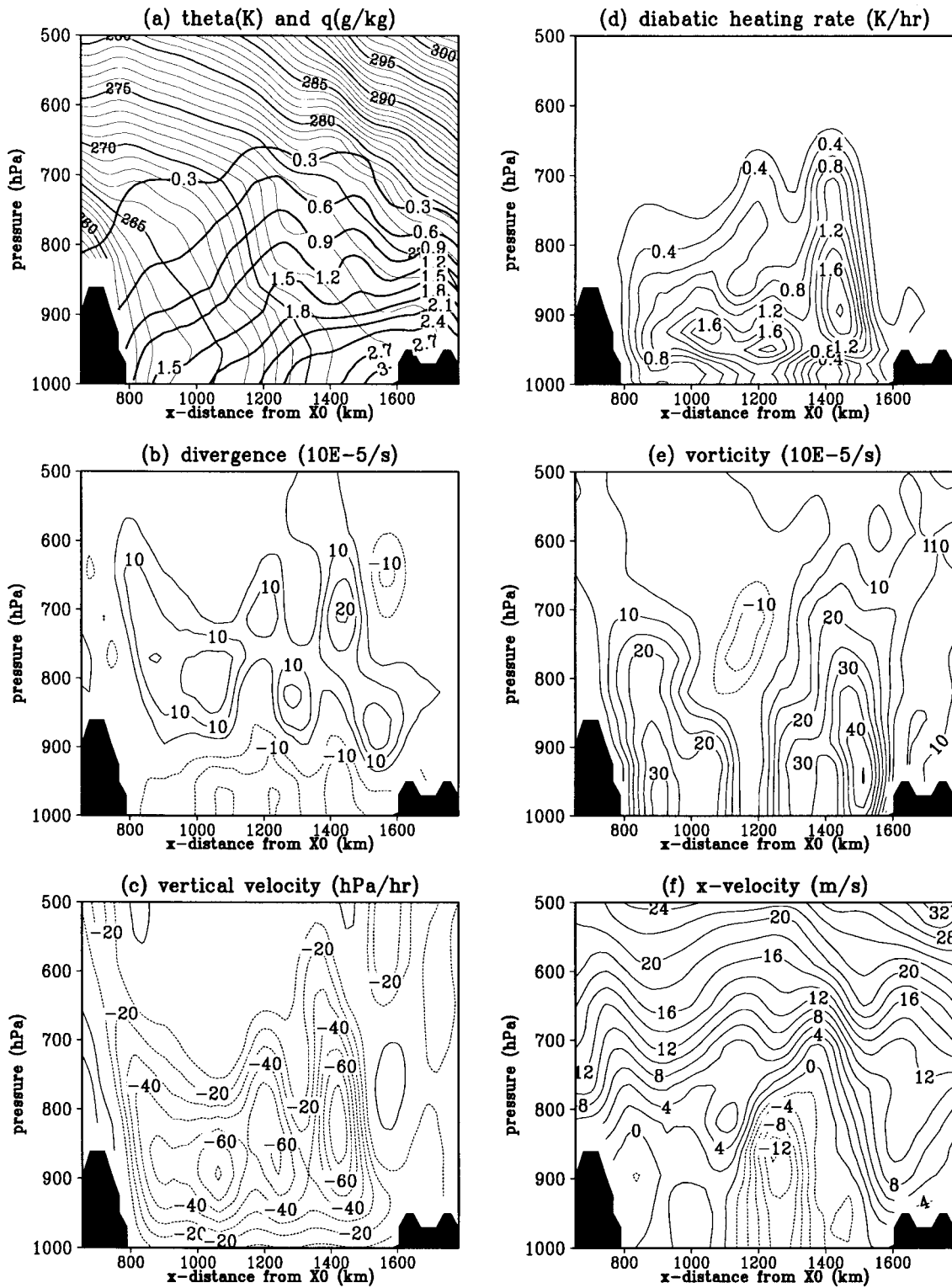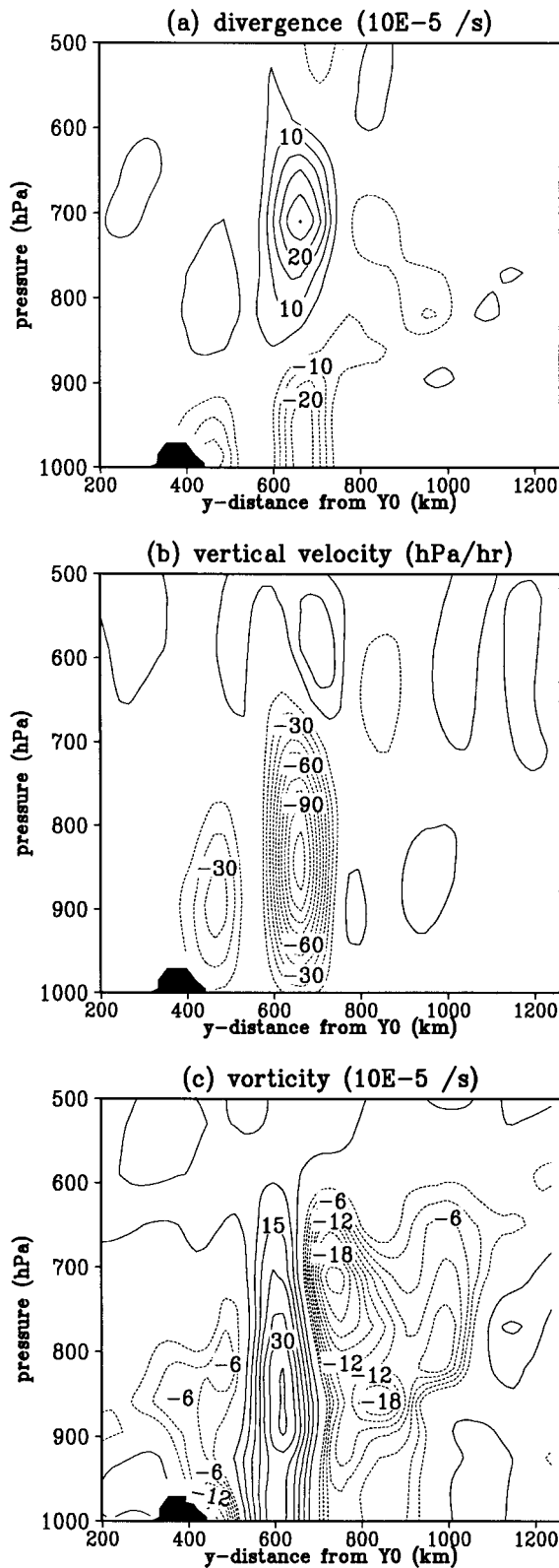
Fig. 12.   Same as Fig. 8, but for at 1200 UTC, 23 January 1990 along the line of $X0 - X1$ in Fig. 11.

(a) divergence (10E-5 /s)

(b) vertical velocity (hPa/hr)

(c) vorticity (10E-5 /s)

heating due to the moist processes is also intense. In comparison to Fig. 8e, vorticity is intensified significantly from 1200 to 1600 km of the abscissa (Fig. 12e). The vorticity also has two maxima between 1200 and 1600 km below 820 hPa. These maxima merge to form a single maximum of vorticity above 820 hPa. The two vortex maxima in the lower level are considered to correspond to the MβCs embedded in the MαC. They are also referred to as the MβC-A and the MβC-B. These results indicate significant development of the MαC with the formation of the MβCs. The negative x-component of velocity is present from 1100 to 1500 km and extends to the level of 800 hPa (Fig. 12f). This causes the warm air advection over the mesoscale cyclones.

The vertical cross-section of horizontal divergence in the y-direction ($Y0 - Y1$ in Fig. 11) shows intense lower-level convergence and upper level divergence at the central part of the MαC (Fig. 13a), where intense vertical velocity extends from the surface to about 650 hPa with a horizontal scale of about 200 km (Fig. 13b). The positive vorticity (Fig. 13c) of the MαC is concentrated in a narrow region with a width of about 200 km and extends to ~700 hPa at the central part of the MαC. This indicates that the flow in the MαC is highly ageostrophic. We consider that these cores of vertical velocity and vorticity correspond to the MβCs. The negative vorticity on the NE side (the right-hand side of the figure) corresponds to the upper-level clockwise circulation. As we mentioned in subsection 4.2, this negative vorticity is a characteristic of the flow field observed when the convergence zone develops.

The time series of the vorticity field at the surface shows that the two MβCs move in different directions within the MαC (Fig. 14). The MβC-A moves to the ENE, while the MβC-B moves to the SE. Their movements are controlled by the circulation of the MαC. The time series of radar images (Fig. 5) also shows that MβC-A moved to the ENE and MβC-B to the

Fig. 13. Vertical cross-sections at 1200 UTC, 23 January 1990 along the line of $Y0$ to $Y1$ in Fig. 11. (a) Horizontal divergence (10^{-5} s^{-1}), (b) vertical velocity (hPa hr^{-1}), and (c) vorticity (10^{-5} s^{-1}).
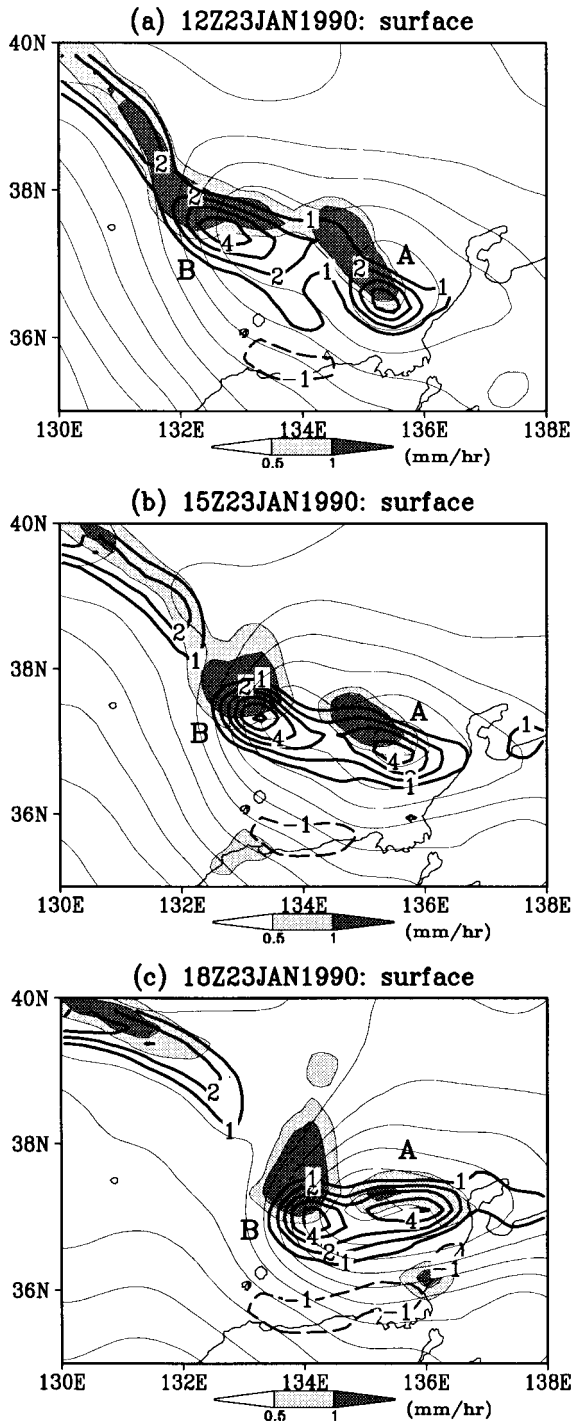
Fig. 14. Time series of vorticity (thick lines; 10^{-5} s^{-1}) at the surface, precipitation intensity (shadings, mm hr^{-1}), and surface pressure (thin lines, hPa). The gray scale of the precipitation intensity is shown at the bottom of each figure. MβCs-A and -B are indicated by "A" and "B" in the figures, respectively.

SE. Their movements are simulated well in the experiment, even though the time and place of the simulated MβCs are not exactly the same as the observed vortices. When the MβCs develop, the horizontal shear is intensified with the development of the MαC. This suggests that the cyclogenesis of the MβCs is related to the intense horizontal shear. As shown by Nagata (1993), we also consider that the cyclogenesis of MβCs is attributed to the hydrodynamic instability of the flow with the intense horizontal shear. Their further development may be related to the lower-level convergence and upward motion. The MβCs are considered as the cores of upward motion and vorticity of the MαC. They are the primary structure of the MαC and strongly contribute to its development.

5. Sensitivity experiments

Since the convergence zone, the MαC, and the MβCs were well simulated with the JSM, we performed a number of numerical sensitivity experiments to elucidate the potential effects of the orography, the heat supply from the sea, and moist processes in the development of the disturbances.

5.1 Effect of the moist processes

In order to examine the effect of the moist processes on the mesoscale cyclones and the convergence zone, we performed an experiment without moist processes under the same conditions as those used in the simulation experiment.

The surface pressure field of the experiment at 1200 UTC, 23 January 1990 (Fig. 15a) shows that the convergence zone forms on the lee side of Mts.C and that the MαC also forms in almost the same place as in the simulation experiment but that the MαC is considerably weaker in magnitude. No MβCs are found within the MαC. At 850 hPa (Fig. 15b), the ageostrophic NE-ward flow is present on the NE side of the convergence zone. The upper-level divergence is, however, considerably weaker. Consequently, the upward vertical velocity is significantly weaker than that of the simulation experiment. This result indicates that the diabatic heating caused by the moist processes intensifies the upward motion and contributes significantly to the development of the MαC.
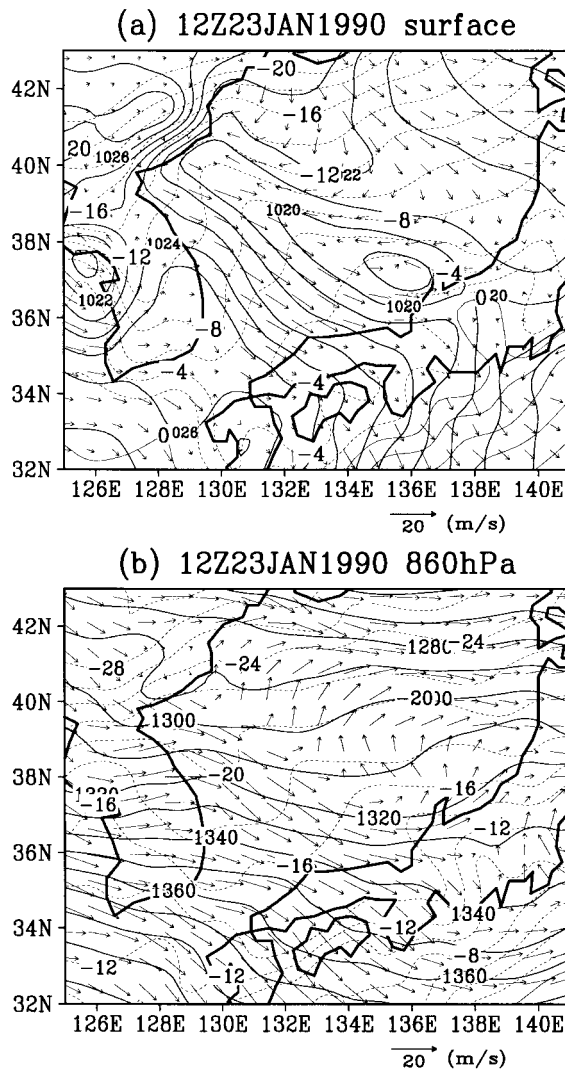
(a) 12Z23JAN1990 surface

(b) 12Z23JAN1990 860hPa

Fig. 15. Horizontal displays of (a) surface pressure (solid lines; unit is hPa), surface wind (arrows; m s^{-1}), and temperature of 1000 hPa (dashed lines; °C), and (b) height (thin solid lines; meter), temperature (dashed lines; °C), and wind (arrows; m s^{-1}) at a level of 860 hPa at 1200 UTC, 23 January 1990 obtained from a sensitivity experiment without moist processes.

5.2 Effect of the sensible heat supplied from the sea

In order to examine the effect of the sensible heat supplied from the sea, we made a sensitivity experiment without sensible heat flux at
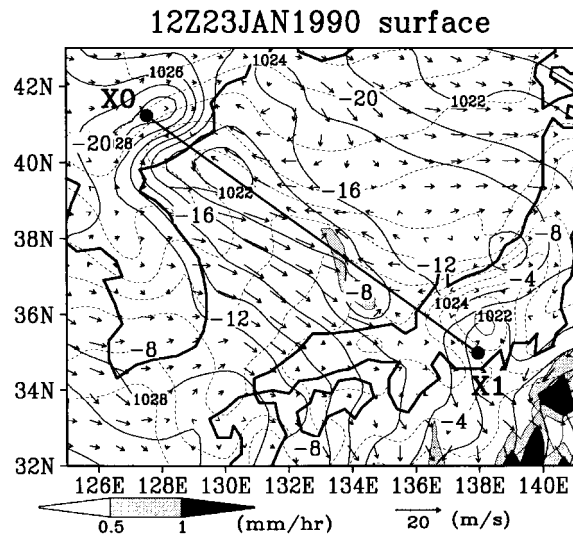
12Z23JAN1990 surface

Fig. 16. Horizontal display of surface pressure field (solid lines; hPa), surface wind (arrows; m s^{-1}), and precipitation intensity (shaded areas; mm hr^{-1}) at 1200 UTC, 23 January 1990 obtained from the experiment without sensible heat flux from the sea.

the surface under the same conditions as those used in the simulation experiment.

In this experiment, the convergence zone forms on the lee side of Mts.C, while the MαC almost disappears (Fig. 16). The heating due to the vertical diffusion in the lower layer is about one-third of that of the simulation experiment, and the heating due to the moist processes is also significantly reduced. As a result, the total diabatic heating is significantly reduced, and the vertical velocity is very small. Consequently, the upper-level divergence is not strong enough to develop the MαC.

In addition to the lack of sensible heat flux, all moist processes are eliminated (Fig. 17). This experiment is almost identical to an experiment without the surface fluxes of both sensible and latent heat because the airflow from the continent is very dry and most of the moisture over the sea is supplied from the sea. Since no diabatic heating occurs over the Sea of Japan, stratification in the lower atmosphere is strongly stable. The airmass, therefore, moves almost horizontally over the sea. As a result, neither the convergence zone nor the MαC is generated, even though Mts.C creates a conflu-
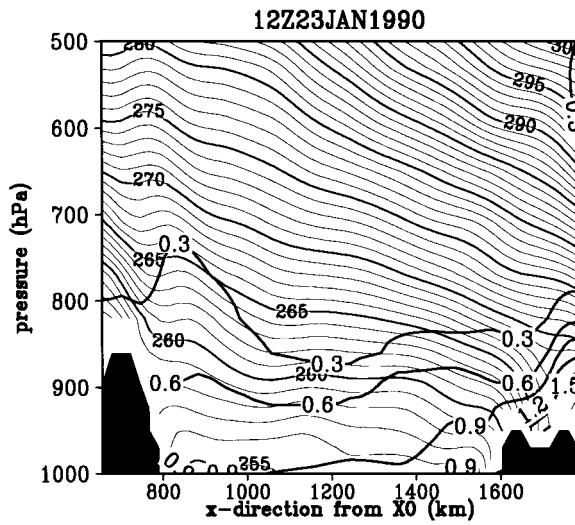
Fig. 17. Vertical cross-section of potential temperature (thin lines; K) and specific humidity (thick lines; g kg^{-1}) along the line of $X0 - X1$ in Fig. 16 at 1200 UTC, 23 January 1990 obtained from the experiment with no sensible heat flux from the sea and no moist processes. Shading in the figure indicates mountains.
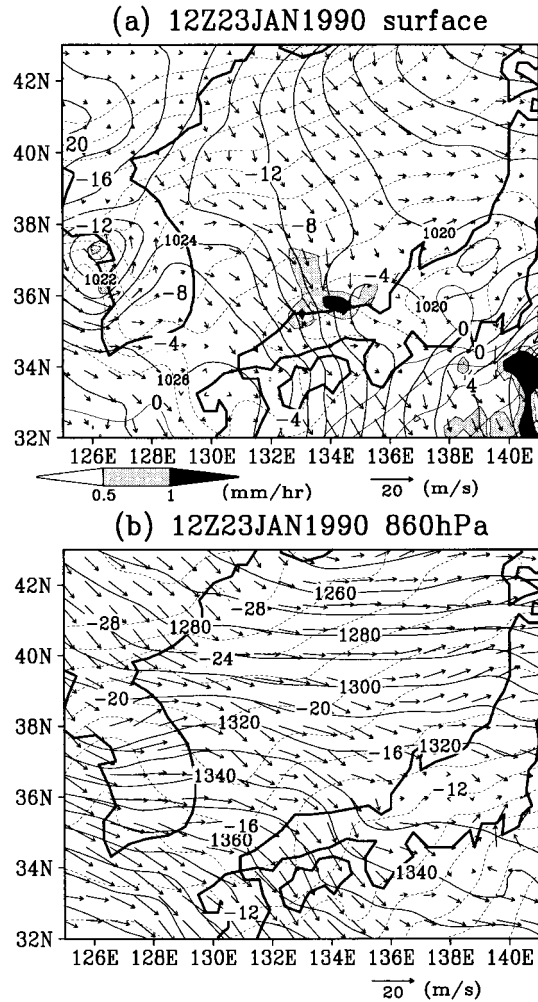

Fig. 18. Horizontal displays at 1200 UTC, 23 January 1990 obtained from the experiment with modified orography. (a) Surface pressure (thick solid lines; unit is hPa), surface wind (arrows; m s^{-1}), temperature of 1000 hPa (thin lines; °C), and precipitation intensity (shaded areas; mm hr^{-1}), and (b) height (solid lines; meter), temperature (dashed lines; °C), and wind (arrows; m s^{-1}) at 860 hPa.

ence on its lee side. Instead, a weak low forms on the lee side of Mts.C by a purely mechanical forcing of the orography. It should be emphasized that the lee cyclone is different from the MαC in the convergence zone.

These results show that the sensible heat flux from the sea surface and the development of a mixing layer with small static stability are necessary for the development of the MαC.

5.3　Role of Mts.C

Mts.C are isolated mountains with a diameter of about 300 km at an altitude of 1000 m; the height of the summit is about 2700 m, as indicated by the rectangle in Fig. 2. In order to examine the role of Mts.C in the formation of mesoscale cyclones, we performed an experiment with a modified orography. In this experiment, mountains higher than 600 m in the rectangle in Fig. 2 were removed, but the same condition as in the simulation experiment was used.

The surface pressure at 1200 UTC, 23 January 1990 (Fig. 18a) shows that neither a significant convergence zone nor a mesoscale cyclone

develops over the Sea of Japan. Precipitation over the Sea of Japan almost disappears. At 860 hPa (Fig. 18b), the flow is almost geostrophic, and no significant divergence occurs. The Sea of Japan is covered with a single airmass with the mixing layer developing below the 850 hPa level, and no significant ascending motion is found over the Sea of Japan.

The significant difference between this experiment and the simulation experiment indicates that Mts.C are a necessary condition for the formation of the convergence zone and mesoscale cyclones.

We made three other experiments, in which all mountains were removed and a bell-shaped mountain was placed at the same position of Mts.C. The bell-shaped mountain $Z(x, y)$ is given by

$$Z(x,y) = Z_{max} \exp\left[-\left\{\left(\frac{x-X_c}{L}\right)^2 \right.\right.$$
$$\left.\left. + \left(\frac{y-Y_c}{L}\right)^2\right\}\right], \qquad (2)$$

where Z_{max} is the height of the summit of the bell-shaped mountain, (X_c, Y_c) is the position of the summit, and L is the horizontal scale of the mountain, taken to be 250 km.

Three different heights Z_{max} of 2000, 1000, and 200 m were used for the experiments (figures are not shown). When the Z_{max} is 2000 m, the surface pressure field shows the convergence zone and the MαC on the lee side of the mountain. The feature of the MαC is essentially the same as that in the simulation experiment. When the Z_{max} is reduced to 1000 m, the convergence zone and the MαC are very weak. Both the convergence zone and the MαC almost disappear for $Z_{max} = 200$ m; this result is similar to that of the experiment with the modified mountain (Fig. 18a). Precipitation over the Sea of Japan is significantly reduced with a decrease in the Z_{max}.

These results indicate that a mountain that is high enough to block and split the air stream is a necessary condition to produce the convergence zone and the MαC on its lee side. They also indicate that no other mountains except Mts.C are essential for the formation and development of the convergence zone and the MαC.

6. Discussion

6.1 Development mechanism of the MαC

The simulation experiment showed that the MαC develops in the zone of preexisting convergence, upward motion, and vorticity. Instead of a linear instability theory, we will discuss the mechanism of lowering the surface pressure of the MαC from the viewpoint of the pressure tendency equation (1).

The time-height cross-section of the area-averaged divergence (Fig. 6a) shows that the upper-level (850∼500 hPa) divergence is maintained during the development of the MαC. This is caused by the ageostrophic NE-ward outflow above the convergence zone (see Figs. 7b, 9f, and 11b). Therefore, the dynamics of the ageostrophic NE-ward outflow will be discussed using the frictionless momentum equation,

$$\frac{d\mathbf{V_h}}{dt} = -f\mathbf{k} \times \mathbf{V_a}, \qquad (3)$$

where $\mathbf{V_h}$ is the horizontal velocity, f is the Coriolis parameter, $\mathbf{k}$ is the vertical unit vector, and $\mathbf{V_a}$ is the ageostrophic velocity. Nagata (1992) performed a trajectory analysis to explain the parcel acceleration to the NE of the convergence zone, while we show the horizontal displays of velocity and acceleration vectors (Fig. 19). As Nagata (1992) examined an air-parcel which moves to the convergence zone from the NE, we also consider movements of air-parcels approaching the MαC from the NE. The acceleration vectors $-f\mathbf{k} \times \mathbf{V_a}$ (solid arrows) rotate the SE-ward velocity of air-parcels clockwise in the north of the MαC at 950 hPa as the air-parcels approach the MαC (Fig. 19c). When they reach the MαC, they are forced to have westward velocity and are lifted up by the intense upward motion in the MαC. The air-parcels with NW-ward velocity, then, are accelerated NE-ward in the upward motion (Fig. 19b). Finally, they obtain NE-ward velocity in the upper-level and cause the upper-level divergence (Fig. 19a).

In order to reveal the dynamics of the formation of the upper-level ageostrophic velocity, we examine the frictionless momentum equation in the same way as Nagata (1992), Nagata and Ogura (1991), and Keyer and Johnson (1984). They analyzed the ageostrophic wind in the isentropic coordinate. We analyzed it in the pressure coordinate because the θ-surface has a large gradient around the MαC. The frictionless momentum equation (3) will be rewritten as

$$\mathbf{V_a} = \frac{1}{f}\mathbf{k} \times \left(\underbrace{\frac{\partial}{\partial t}}_{LT} + \underbrace{\mathbf{V_h} \cdot \nabla_p}_{IA} + \underbrace{\omega\frac{\partial}{\partial p}}_{ID}\right)\mathbf{V_h}, \qquad (4)$$

where Terms LT, IA, and ID are the local ten-

(a) 770hPa:divergence(10E−5/s)

(b) 860hPa: omege(hPa/hr)
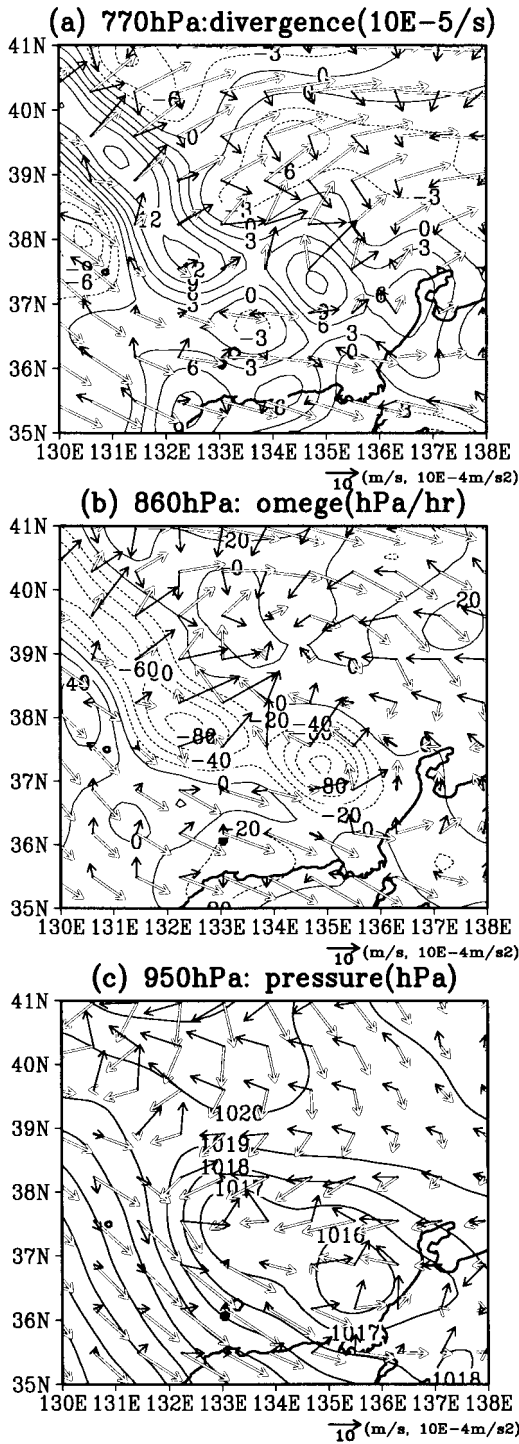
(c) 950hPa: pressure(hPa)

Fig. 19. Horizontal velocity vectors (open arrows; m s^{-1}) and their acceleration (solid arrows; 10^{-4} m s^{-2}) at (a) 770 hPa, (b) 860 hPa, and (c) 950 hPa. Contours are (a) divergence (10^{-5} s^{-1}), (b) vertical velocity (hPa hr^{-1}), and (c) surface pressure (hPa) at 1200 UTC, 23 January 1990 in the simulation experiment.

dency, inertial advective, and inertial diabatic components, respectively. If $\mathbf{V_h}$ is approximated by the geostrophic velocity $\mathbf{V_g}$, then, the geostrophic momentum approximation form is obtained as

$$\mathbf{V_a} = \frac{1}{f}\mathbf{k} \times \underbrace{\left(\frac{\partial}{\partial t} + \underbrace{\mathbf{V_h} \cdot \nabla_p}_{IA} + \underbrace{\omega\frac{\partial}{\partial p}}_{ID}\right)}_{LT} \mathbf{V_g}. \qquad (5)$$

Figure 20 shows the ageostrophic velocity vectors of the total form and each component and divergence of the individual components. The total ageostrophic velocity is compared with the ageostrophic velocity calculated from $\mathbf{V_a} = \mathbf{V_h} - \mathbf{V_g}$ (Fig. 20a). This shows that they almost agree with each other, and the ageostrophic velocity calculated from (4) gives a good approximation. The divergence of the total ageostrophic velocity at 770 hPa is significant above the MαC, which is responsible for lowering the surface pressure. The local tendency (Term LT) has no significant divergence above the central part of the MαC (Fig. 20b). The divergence of the inertial advective component (Term IA) is significant in the northern side of the MαC (Fig. 20c). On the other hand, the inertial diabatic component (Term ID) has two significant maxima of divergence (Fig. 20d); one is located at the central part of the MαC, and the other is on its NW-side. Term ID is, therefore, most responsible for lowering the surface pressure of the MαC, while Term IA also contributes to the cyclone development. Comparing Term IA in (4) with that of the geostrophic momentum approximation (5), a large difference in the patterns is found (Figs. 20c and 20e). This indicates that most of the divergence in Fig. 20c is attributed to the horizontal momentum advection of the ageostrophic component ($\mathbf{V_h} \cdot \nabla\mathbf{V_a}$). On the other hand, the divergence pattern of Term ID (Fig. 20d) is similar to that of the geostrophic momentum approximation (Fig. 20f), while its magnitude is slightly small. This indicates that the vertical advection of the geostrophic momentum ($\omega(\partial\mathbf{V_g}/\partial p)$) significantly contributes to the formation of ageostrophic velocity and its divergence. Since $\partial\mathbf{V_g}/\partial p$ is related to the baroclinicity of the troposphere, the ageostrophic velocity formation intensifies with more intense baroclinicity and with more intense upward
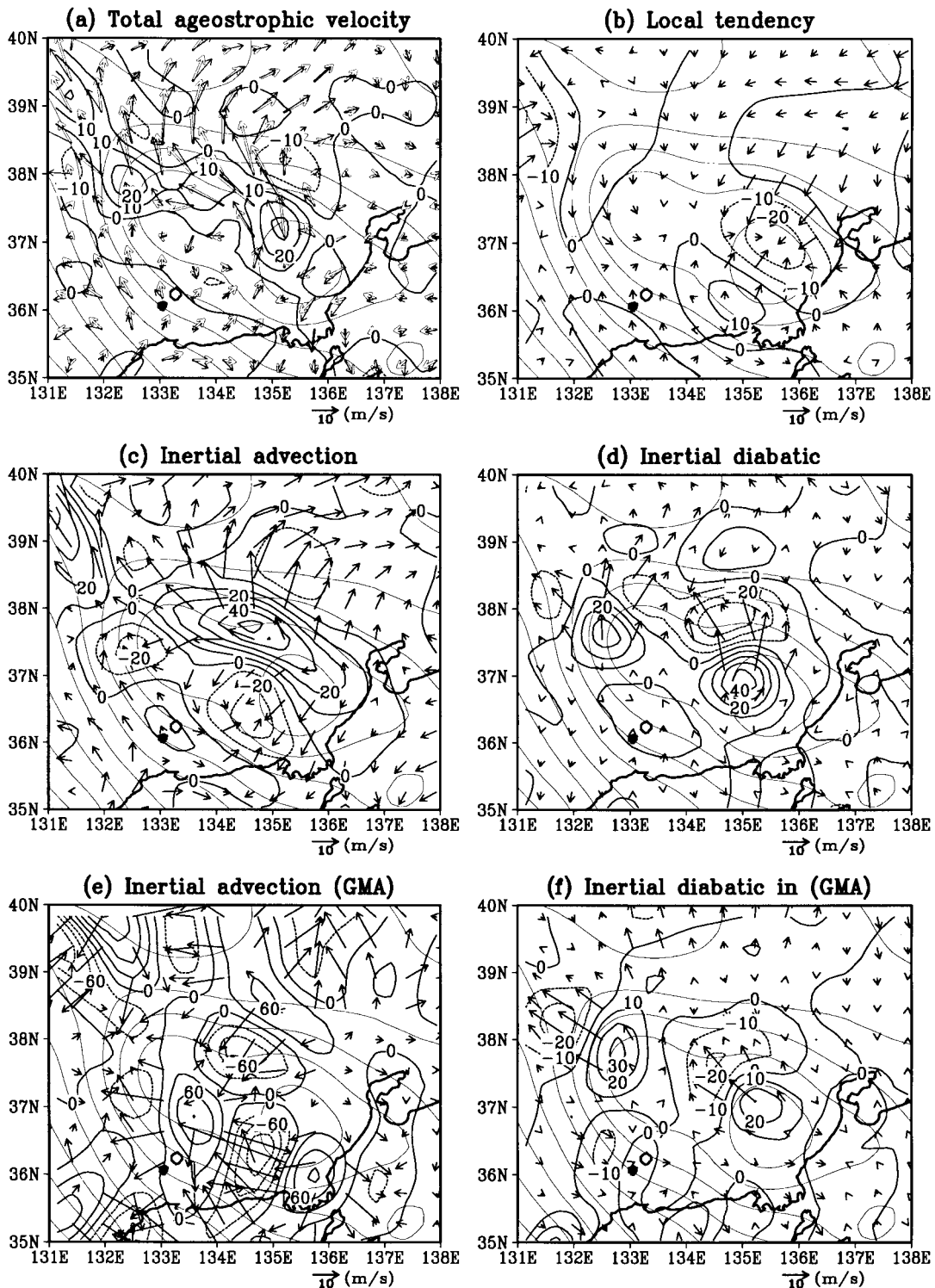
Fig. 20. Ageostrophic velocity vectors at 770 hPa at 1200 UTC, 23 January 1990 in the simulation experiment. (a) Total ageostrophic velocity vectors calculated from the momentum equation (open arrows) and those from $\mathbf{V_a} = \mathbf{V_h} - \mathbf{V_g}$ (solid arrows), (b) local tendency component, (c) inertial advective component, (d) inertial diabatic component, (e) inertial advective component in the geostrophic momentum approximation (GMA), and (f) inertial diabatic component in the geostrophic momentum approximation. The thick contour lines are the divergence (10^{-5} s^{-1}) of each component, and thin contours are the surface pressure.
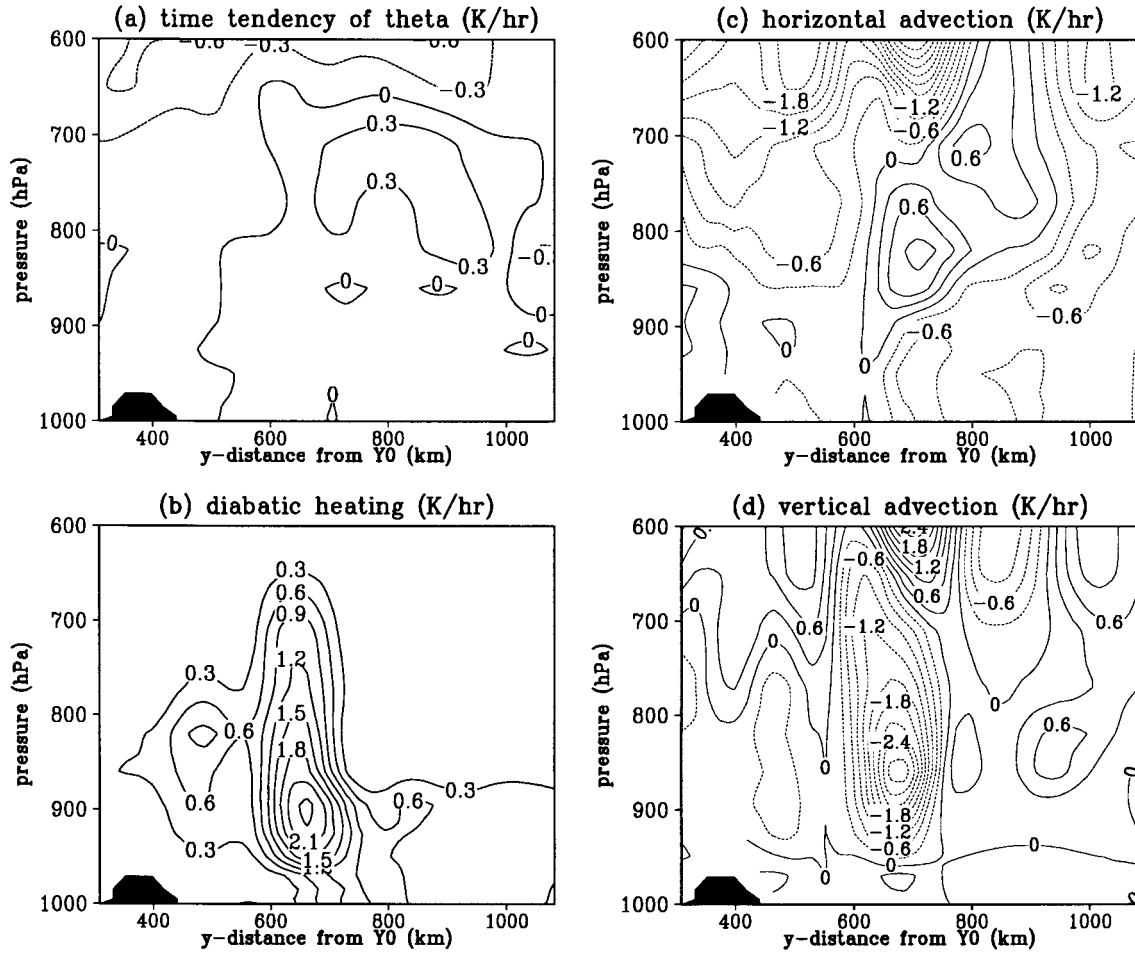
(a) time tendency of theta (K/hr)

(c) horizontal advection (K/hr)

(b) diabatic heating (K/hr)

(d) vertical advection (K/hr)

Fig. 21. Vertical cross-sections of heating rates (K hr^{-1}) along the line of $Y0 - Y1$ in Fig. 11 at 1200 UTC, 23 January 1990 in the simulation experiment. (a) Local time tendency, (b) diabatic component, (c) horizontal advection of θ, and (d) vertical advection of θ. Shading in the figures indicates mountains.

motion. In the present case, the synoptic charts (Fig. 3) show that the baroclinicity is intense over the Sea of Japan.

The next question is the dynamics of the intense upward motion within the MαC. Since we consider the hydrostatic system, buoyancy due to diabatic heating is not explicitly related to the upward motion. We, therefore, discuss the intensity of upward motion using the thermodynamic equation,

$$\frac{\partial \theta}{\partial t} = \underbrace{-\mathbf{V_h} \cdot \nabla_p \theta}_{HA} + \underbrace{\frac{\theta}{C_p T} \dot{Q}}_{DH} - \underbrace{\omega \frac{\partial \theta}{\partial p}}_{VA}, \qquad (6)$$

where C_p is the specific heat at constant pressure, T is the temperature, and $\dot{Q}$ is the diabatic heating rate. In this study, $\dot{Q}$ is mainly caused by the moist processes and the vertical diffusion. The terms HA, DH, and VA indicate the horizontal advection of θ, the diabatic heating, and the vertical advection of θ, respectively. Figure 21 shows vertical cross-sections of each term of (6) obtained in the simulation experiment at 12 UTC, 23 January. In this case, the diabatic heating (Term DH) and horizontal advection (Term HA) are almost in balance with the negative vertical advection of θ (Term VA). The local tendency $\partial \theta / \partial t$ is caused

by the residual heating. This result suggests that the thermodynamic equation (6) may be approximated as

$$
\underbrace{-\mathbf{V_h} \cdot \nabla_p \theta}_{HA} + \underbrace{\frac{\theta}{C_p T}\dot{\mathbf{Q}}}_{DH} \approx \underbrace{\omega \frac{\partial \theta}{\partial p}}_{VA}, \tag{7}
$$

to discuss the relationship between the heating and the vertical velocity, ω. In the case of the present MαC, the diabatic heating (Term DH) is large because of the large sensible and latent heat fluxes and the latent heat release (Fig. 21b, see also Fig. 12d). In the upper-level (900~750 hPa) above the MαC, the ageostrophic wind is significant and causes warm air advection (Figs. 11b and 12f). This causes the positive value of Term HA (Fig. 21c). On the other hand, $\partial\theta/\partial p$ is small because of the development of the deep mixing layer (Fig. 12a). All these factors result in large upward velocity to maintain the large negative vertical advection of θ (Term VA) (Fig. 21d).

In the experiment without moist processes, the diabatic heating is caused mainly by the vertical diffusion. This decrease of $\dot{\mathbf{Q}}$ results in the reduction of the upward velocity to one half of that of the simulation experiment. As a result, the MαC is very weak (Fig. 15). If the surface sensible heat flux is switched off, the mixing layer is shallow, and $\partial\theta/\partial p$ becomes large in the lower level. In this case, the condensation heating is also strongly suppressed. Consequently, the upward velocity becomes very weak, and the MαC dose not develop (Fig. 16). When both the moist processes and the surface sensible heat flux are switched off, the mixing layer dose not develop and no upward motion occurs (Fig. 17).

From these discussion, the development mechanism of the MαC is summarized as follows. The moist precesses and the surface heating intensify the preexisting upward motion that develops in the convergence zone. The upward motion in the baroclinic environment causes the ageostrophic velocity in the upper level. The horizontal advection of ageostrophic momentum also contributes to intensifying the upper-level ageostrophic velocity. The intense divergence of the ageostrophic velocity in the upper level results in decreasing the surface pressure and the development of the MαC.

6.2 The secondary upward motion

The simulation experiment shows that a weak secondary upward motion is present on the NE side of the convergence zone (Fig. 9c). Arakawa et al. (1988) observed the secondary upward motion to the NE of the main upward motion (Fig. 10). Nagata (1991) made numerical experiments of the convergence zone and pointed out that the negative vorticity on the NE side of the convergence zone reduces the horizontal inertial stability. In order to examine the dynamic stability of the region where the secondary upward motion occurs, vertical cross-sections of the geostrophic absolute momentum ($M = u_g - fy$), potential temperature (θ), and vertical velocity are shown in Fig. 22, where u_g is the x-component of geostrophic velocity. The variables are averaged in the x-direction between $P0$ and $P1$ in Fig. 7.

At 00 UTC, 23 January (Fig. 22a), the convergence zone is located around $y = 500$ km, with the main upward motion below 700 hPa. On the NE side (right-hand side of the figure) of the convergence zone, the secondary upward motion is present from 600 to 800 km in the y-coordinate and from 900 to 550 hPa. In this region, the M-surface is almost horizontal or weakly leaning, and its gradient is smaller or almost the same as that of θ. At 12 UTC, 23 January (Fig. 22b), the secondary upward motion is present from 780 to 900 km in the y-coordinate and from 800 to 650 hPa. In this region, the M-surface is more inclined than the θ-surface. These characteristics of M and θ fields suggest that symmetric instability is expected in the region. This could be a possibility to explain the weak secondary upward motion on the NE side of the intense main upward motion along the convergence zone (Fig. 9c). The satellite image (Fig. 4a) shows that some transversal cloud lines are embedded in the broad cloud band. We infer that they could be caused by the ageostrophic NE-ward flow with the weak upward motion.

6.3 Multi-scale structure of mesoscale cyclones

The time series of satellite images (Fig. 4) and radar images (Fig. 5) shows the different movements of the two MβCs. The simulation experiment also showed that MβC-A moved ENE-ward and MβC-B, SE-ward (Fig. 14). The MβCs are embedded in the MαC, and their
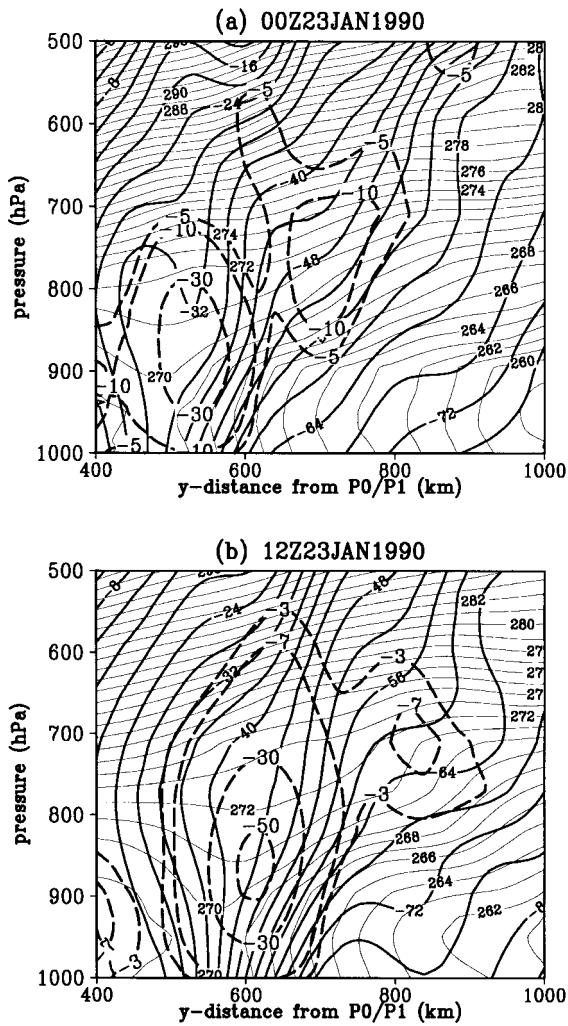
(a) 00Z23JAN1990

(b) 12Z23JAN1990

Fig. 22. Vertical cross-sections of geostrophic absolute momentum $M = u_g - fy$ (thick lines; m s^{-1}), potential temperature (thin lines; K), and vertical velocity (dashed lines; hPa hr^{-1}) in the simulation experiment at (a) 0000 UTC and (b) 1200 UTC, 23 January 1990, where u_g is the x-component of geostrophic horizontal velocity, f is the Coriolis parameter, and y is the horizontal distance. Variables are averaged in the x-direction from $P0$ to $P1$ indicated in Fig. 7.

movements are controlled by the cyclonic rotation of the MαC.

The simulation experiment showed that horizontal shear intensifies with the development of the MαC. This means that the MαC provides an environmental field for the cyclogenesis

of the MβCs. In the case of Nagata (1993), the convergence zone had a horizontal shear that was strong enough to produce the MβCs. The horizontal scale and vertical extent of the MβCs are almost the same as those in Nagata (1993). The MβCs of the present study also develop along a strong shear zone. We infer that the mechanisms of their cyclogenesis are essentially the same as those in Nagata (1993).

On the other hand, the MβCs constitute the main components of the MαC. As shown in Fig. 13, intense divergence, vertical motion (ω), and vorticity are concentrated within the MβCs. The inertial diabatic component (Term ID) also mainly occurred within the two MβCs (Fig. 20). These facts indicate that the MβCs are considered as the cores of the MαC and significantly contribute to lowering the pressure of the MαC. These results show that the MαC and MβCs have a close interaction.

7. Summary and conclusions

Mesoscale cyclones are frequently observed in the western Sea of Japan when there is an outburst of cold air (Asai 1988). In this region, a convergence zone forms on the lee side of the mountains north of Korea (Mts.C). Mesoscale cyclones occasionally develop along the convergence zone. A meso-α-scale cyclone (MαC) was observed by satellite on 23 January 1990. The JMA meteorological radars at Fukui and Niigata showed that two meso-β-scale cyclones (MβCs) were embedded in the MαC. This structure is referred to as "the multi-scale structure" of mesoscale cyclones.

In order to clarify the multi-scale structure and the development mechanism of mesoscale cyclones, we performed a simulation experiment and a number of sensitivity experiments with respect to several factors using JSM.

The convergence zone forms on the lee side of Mts.C over the Sea of Japan after the synoptic-scale low moves NE-ward. It is characterized by a mesoscale surface trough with lower-level convergence and upper-level (800~600 hPa) divergence, intense upward motion, and positive vorticity. The mesoscale cyclones develop in the region of the preexisting upward motion and vorticity. We discussed the development mechanism of the MαC from the viewpoint of the pressure tendency equation and the intensification of the upper-level divergence.

Since the differences in the temperatures of the sea and the atmosphere are large, large amounts of sensible heat and latent heat are supplied from the sea to the atmosphere. Diabatic heating and the horizontal advection of θ nearly balance the negative vertical advection of θ. The local temperature increase is caused by residual heating. Using the thermodynamic equation, it was shown that the balance results in the intense upward motion because the $\partial\theta/\partial p$ is small in the mixing layer. Since the baroclinicity in this region is intense, upward transfer of the geostrophic momentum around the convergence zone intensifies the upper-level divergence. Consequently, the MαC forms and develops. The upward motion and vorticity are confined mostly within the MβCs, which are considered as the cores of the MαC disturbance. On the other hand, the MαC provides a favorable environment for the formation and development of the MβCs and affects their movements.

The present study showed that the upward transfer of momentum as well as heat is important for the formation of mesoscale cyclones. This suggests that a numerical study using a cloud-resolving model is necessary for a further study of mesoscale cyclones in the future. In particular, the development process and detailed dynamics of the MβCs should be studied by the cloud-resolving non-hydrostatic model. Many types of mesoscale cyclones and vortices are observed over the Sea of Japan. The horizontal scales of mesoscale cyclones range from a few tens of kilometers to several hundred kilometers. Further observational and numerical studies are necessary to clarify their structures and mechanisms.

Acknowledgements

References

Arakawa, S. and Research Group on Mesoscale Meteorology of Marine Development, JMA, 1988: On the mesoscale structure of the cloud band system over the Japan Sea in winter monsoon period.—A mesoscale observation on board R/V Keifu-Maru. (in Japanese) *Tenki*, **35**, 237–248.

Asai, T., 1988: Mesoscale features of heavy snowfalls in Japan Sea coastal regions of Japan. (in Japanese) *Tenki*, **35**, 156–161.

Bratseth, A.M., 1985: A note on CISK in polar air masses. *Tellus*, **37A**, 403–406.

Businger, S., 1985: The synoptic climatology of polar low outbreaks. *Tellus*, **37A**, 419–432.

———, 1987: The synoptic climatology of polar low outbreaks over the Gulf of Alaska and the Bering Sea. *Tellus*, **39A**, 307–325.

——— and G. Walter, 1988: Comma cloud development and associated rapid cyclogenesis over the Gulf of Alaska: A case study using aircraft and operational data. *Mon. Wea. Rev.*, **116**, 1103–1123.

Craig, G. and Han-Ru Cho, 1988: Cumulus heating and CISK in the extratropical atmosphere. Part I: Polar lows and comma clouds. *J. Atmos. Sci.*, **45**, 2622–2640.

Duncan, C.N., 1977: A numerical investigation of polar lows. *Quart. J. Roy. Meteor. Soc.*, **103**, 255–267.

Emanuel, K.A., 1986: An air-sea interaction theory for tropical cyclones. Part I: Steady-state maintenance. *J. Atmos. Sci.*, **43**, 585–604.

——— and R. Rotunno, 1989: Polar lows as arctic hurricanes. *Tellus*, **41A**, 1–17.

Harrold, T.W. and K.A. Browning, 1969: The polar low as a baroclinic disturbance. *Quart. J. Roy. Meteor. Soc.*, **95**, 710–723.

Iga, K., 1993: Reconsideration of Orlanski's instability theory of frontal waves. *J. Fluid Mech.*, **255**, 213–236.

———, 1997: Instability of a front with a layer of uniform potential vorticity. *J. Meteor. Soc. Japan*, **75**, 1–11.

Kerser, D.A. and D.R. Johnson, 1984: Effects of diabatic heating on the ageostrophic circulation of an upper tropospheric jet streak. *Mon. Wea. Rev.*, **112**, 1709–1724.

Mansfield, D.A., 1974: Polar lows: The development of baroclinic disturbances in cold air outbreaks. *Quart. J. Roy. Meteor. Soc.*, **100**, 541–554.

Mellor, G.L. and T. Yamada, 1974: A hierarchy of turbulence closure models for planetary boundary layers. *J. Atmos. Sci.*, **31**, 1791–1806.

Moore, G.W.K., M.C. Reader, J. York and S. Sathiyamoorthy, 1996: Polar lows in the Labrador Sea: A case study. *Tellus*, **48A**, 17–40.

Nagata, M., M. Ikawa, S. Yoshizumi and T. Yoshida, 1986: On the formation of a convergent cloud band over the Japan Sea in winter: Numerical experiments. *J. Meteor. Soc. Japan*, **64**, 841–855.

———, 1987: On the structure of a convergent cloud band over the Japan Sea in winter: A prediction experiment. *J. Meteor. Soc. Japan*, **65**, 871–883.

———, 1991: Further numerical study on the formation of the convergent cloud band over the Japan Sea in winter. *J. Meteor. Soc. Japan*, **69**, 419–428.

——— and Y. Ogura, 1991: A modeling case study of interaction between heavy precipitation and a low-level jet over Japan in the Baiu season. *Mon. Wea. Rev.*, **119**, 1309–1336.

———, 1992: Modeling case study of the Japan-Sea convergent cloud band in a varying large-scale environment: Evolution and upscale effect. *J. Meteor. Soc. Japan*, **70**, 649–671.

———, 1993: Meso-β-scale vortices developing along the Japan-Sea Polar-Airmass Convergence Zone (JPCZ) cloud band: Numerical simulation. *J. Meteor. Soc. Japan*, **71**, 43–57.

Ninomiya, K., 1989: Polar/comma-cloud lows over the Japan Sea and the Northwestern Pacific in winter. *J. Meteor. Soc. Japan*, **67**, 83–97.

———, K. Hoshino and K. Kurihara, 1990: Evolution process and multi-scale structure of a polar-low developed over the Japan Sea on 11–12 December 1985. Part I: Evolution process and meso-α-scale structure. *J. Meteor. Soc. Japan*, **68**, 293–306.

——— and ———, 1990: Evolution process and multi-scale structure of a polar-low developed over the Japan Sea on 11–12 December 1985. Part II: Evolution process and meso-β-scale polar low. *J. Meteor. Soc. Japan*, **68**, 307–318.

Økland, H., 1987: Heating by organized convection as a source of polar low intensification. *Tellus*, **39A**, 397–407.

Ookubo, A., 1995: Two types of vortical disturbances over the Hokuriku district in winter. (in Japanese) *Tenki*, **42**, 705–714.

Orlanski, I., 1968: Instability of frontal waves. *J. Atmos. Sci.*, **25**, 178–200.

Rasmussen, E., 1979: The polar low as an extratropical CISK-disturbance. *Quart. J. Roy. Meteor. Soc.*, **105**, 531–549.

———, 1985: A case study of a polar low development over the Barents Sea. *Tellus*, **37A**, 407–418.

——— and M. Lystad, 1987: The Norwegian Polar Lows Project: A summary of the International Conference on Polar Lows, 20–23 May 1986. Oslo, Norway. *Bull. Amer. Meteor. Soc.*, **68**, 801–816.

Reed, R.J., 1979: Cyclogenesis in polar air streams. *Mon. Wea. Rev.*, **107**, 38–52.

——— and W. Blier, 1986a: A case study of comma cloud development in the Eastern Pacific. *Mon. Wea. Rev.*, **114**, 1681–1695.

——— and W. Blier, 1986b: A further study of comma cloud development in the Eastern Pacific. *Mon. Wea. Rev.*, **114**, 1696–1708.

——— and C.N. Duncan, 1987: Baroclinic instability as a mechanism for the serial development of polar lows: a case study. *Tellus*, **39A**, 376–384.

Sardie, J.M. and T.T. Warner, 1985: A numerical study of the development mechanisms of polar lows. *Tellus*, **37A**, 460–477.

Segami, A., K. Kurihara, H. Nakamura, M. Ueno, I. Takano and Y. Tatsumi, 1989: Operational mesoscale weather prediction with Japan Spectral Model. *J. Meteor. Soc. Japan*, **67**, 907–924.

Tatsumi, Y., 1986: A spectral limited-area model with time-dependent lateral boundary conditions and its application to a multi-level primitive equation model. *J. Meteor. Soc. Japan*, **64**, 637–664.

Tsuboki, K. and G. Wakahama, 1992: Mesoscale cyclogenesis in winter monsoon air streams: Quasi-geostrophic baroclinic instability as a mechanism of the cyclogenesis off the west coast of Hokkaido Island, Japan. *J. Meteor. Soc. Japan*, **70**, 77–93.